Early Science with the Large Millimeter Telescope: COOL BUDHIES I – a pilot study of molecular and atomic gas at $z \simeq 0.2$

Ryan Cybulski,[1]⋆ Min S. Yun,[1]⋆ Neal Erickson,[1] Victor De la Luz,[2]
Gopal Narayanan,[1] Alfredo Montaña,[3,4] David Sánchez,[3] Jorge A. Zavala,[3]
Milagros Zeballos,[3] Aeree Chung,[5] Ximena Fernández,[6,7] Jacqueline van Gorkom,[6]
Chris P. Haines,[8] Yara L. Jaffé,[9,10] María Montero-Castaño,[11] Bianca M. Poggianti,[12]
Marc A. W. Verheijen,[13] Hyein Yoon,[5] Boris Z. Deshev,[13,14,15] Kevin Harrington,[1]
David H. Hughes,[3] Glenn E. Morrison,[16,17] F. Peter Schloerb[1] and Miguel Velazquez[3]

Affiliations are listed at the end of the paper

ABSTRACT

An understanding of the mass build-up in galaxies over time necessitates tracing the evolution of cold gas (molecular and atomic) in galaxies. To that end, we have conducted a pilot study called CO Observations with the LMT of the Blind Ultra-Deep H I Environment Survey (COOL BUDHIES). We have observed 23 galaxies in and around the two clusters Abell 2192 ($z = 0.188$) and Abell 963 ($z = 0.206$), where 12 are cluster members and 11 are slightly in the foreground or background, using about 28 total hours on the Redshift Search Receiver on the Large Millimeter Telescope (LMT) to measure the $^{12}CO\,J = 1 \rightarrow 0$ emission line and obtain molecular gas masses. These new observations provide a unique opportunity to probe *both* the molecular and atomic components of galaxies as a function of environment beyond the local Universe. For our sample of 23 galaxies, nine have reliable detections (S/N $\geq$ 3.6) of the ^{12}CO line, and another six have marginal detections (2.0 < S/N < 3.6). For the remaining eight targets we can place upper limits on molecular gas masses roughly between 10^9 and $10^{10}\,M_{\odot}$. Comparing our results to other studies of molecular gas, we find that our sample is significantly more abundant in molecular gas overall, when compared to the stellar and the atomic gas component, and our median molecular gas fraction lies about 1σ above the upper limits of proposed redshift evolution in earlier studies. We discuss possible reasons for this discrepancy, with the most likely conclusion being target selection and Eddington bias.

Key words: galaxies: clusters: general – galaxies: evolution – galaxies: ISM – infrared: galaxies.

1 INTRODUCTION

One of the most important goals of modern astrophysics is to understand how galaxies have evolved over cosmic time. One can approach this goal by examining the morphologies, stellar mass build-up, colours, and star formation histories of galaxies as a function of redshift. A number of studies along these lines have also revealed that the properties of galaxies strongly depend on local environment, as galaxies residing in regions of higher density at $z \leq$ 1 are more frequently massive, early-type, and passively-evolving (e.g. Dressler 1980; Treu et al. 2003; Poggianti et al. 2006; Haines

et al. 2007; Gallazzi et al. 2009; Tran et al. 2009; Gavazzi et al. 2010; Mahajan, Haines & Raychaudhury 2010; Jaffé et al. 2011; Rasmussen et al. 2012; Scoville et al. 2013; Cybulski et al. 2014). However, it is also fundamentally important to examine how the evolution of gas in the interstellar medium (ISM) of galaxies impacts the growth of stellar mass over cosmic time and as a function of environment. A key observational tool for these efforts is the cold gas content of galaxies, both the atomic (H I) and the molecular (H$_2$, commonly traced by the line emission of the ^{12}CO, hereafter referred to as CO, molecule) components, as stars form in galaxies from the giant molecular clouds that arise out of the cold ISM. The molecular component of the cold ISM, which is found to be more centrally concentrated in spiral discs, tends to more closely trace the sites of recent star formation activity than the H I gas, which is

more extended and loosely bound to the galactic disc (see Young & Scoville 1991, and references therein).

Studies of the total cold ISM, molecular and atomic, in galaxies have historically been relegated to the very local Universe (at distances $\lesssim 100\ h^{-1}$ Mpc), with most of the environmental studies focusing on the Virgo cluster and Coma supercluster (e.g. Haynes, Giovanelli & Chincarini 1984; Giovanelli & Haynes 1985; Gavazzi 1987; Kenney & Young 1989; Casoli et al. 1996; Boselli et al. 1997, 2014; Gavazzi et al. 2006; Pappalardo et al. 2012; Scott et al. 2013). These studies generally found strong evidence for the H I gas being more readily stripped in the cluster environment than the molecular component, when using field galaxies as a baseline. Fabello et al. (2011) showed, by H I stacking on the Arecibo Legacy Fast ALFA survey (Giovanelli et al. 2005), that galaxies at $z \leq 0.06$ exhibit distinct atomic gas deficiencies in environments of higher local density.

Observations of the cold molecular ISM in galaxies have begun extending to higher redshifts (e.g. Daddi et al. 2010; Aravena et al. 2012; Krips, Neri & Cox 2012; Magdis et al. 2012; Bauermeister et al. 2013; Carilli & Walter 2013; Combes et al. 2013; Hodge et al. 2013), and to probe higher density environments, including luminous infrared galaxies (LIRGs) in the outskirts of intermediate-redshift clusters (Geach et al. 2009, 2011; Jablonka et al. 2013), but H I observations are much more scarce at intermediate redshifts. The *GALEX* Arecibo SDSS Survey (GASS; Catinella et al. 2010, 2012, 2013) consists of approximately 800 galaxies at $z \leq 0.05$ with stellar masses $M_* \gtrsim 10^{10}\ \mathrm{M_\odot}$, which have the benefit of uniformly derived stellar masses, star formation rates (SFRs), and atomic gas masses. Furthermore, the CO Legacy Database for the GASS (COLD GASS; Saintonge et al. 2011) has added new molecular gas measurements for a sub-sample of 366 galaxies in GASS. At higher redshift, a study by Lah et al. (2009) of the galaxy cluster Abell 370 ($z = 0.37$) stacked on the positions of more than 300 galaxies, with known spectroscopic redshifts, using 21cm observations with the Giant Metrewave Radio Telescope. The H I stacks place constraints on the average atomic gas mass of galaxies in this cluster, and indicate that the cluster members are generally more gas rich than their counterparts in clusters at lower redshift. The HIGHz survey (Catinella et al. 2008; Catinella & Cortese 2015) used the Arecibo telescope to measure H I in 39 galaxies at redshifts $0.17 \leq z \leq 0.25$, specifically targeting isolated galaxies with large gas reservoirs. The COSMOS HI Large Extragalactic Survey (CHILES; Fernández et al. 2013) is surveying a portion of the COSMOS (Scoville et al. 2007) field with the Jansky Very Large Array, and with sufficient sensitivity to detect atomic gas in galaxies out to $z \sim 0.5$. Initial results from the CHILES project include the detection of 21cm emission from a galaxy at $z \simeq 0.37$ (Fernández et al., submitted).

In recent years, simulations of the gas content in galaxies have begun to predict, using semi-analytic (e.g. Obreschkow et al. 2009; Lagos et al. 2011, 2014; Popping, Somerville & Trager 2014; Popping, Behroozi & Peeples 2015) or hydrodynamical (e.g. Davé, Finlator & Oppenheimer 2012; Davé et al. 2013; Rafieferantsoa et al. 2015) prescriptions, how gas evolves in galaxies over time. One of the most important unanswered questions is how the atomic gas content of galaxies evolves with time relative to the molecular gas. Popping et al. (2014), and others, have shown that changes in model assumptions can yield dramatically different evolution of the molecular-to-atomic gas ratios in galaxies, and the lingering uncertainties regarding the abundances of these cold gas components significantly obfuscate our theoretical understanding of galaxy evolution. These model uncertainties underscore a need for observations of the total cold gas content of the ISM that extend

beyond the local Universe, and which sample a range of galaxy environments.

To address the observational need for measurements of atomic gas in galaxies at intermediate redshifts, and at higher density environments, we have carried out an unprecedented study of the atomic gas, stellar populations, morphology, and star formation activities of two galaxy clusters at $z \sim 0.2$ and their surrounding large-scale structure. Our project, the Blind Ultra-Deep H I Environmental Survey (BUDHIES; Verheijen et al. 2007, 2010; Jaffé et al. 2012, 2013, 2015), consists of multiwavelength observations covering an area of 1×1 deg^2 (~ 100 Mpc^2) around the two clusters Abell 2192 ($z = 0.188$, RA=16:26:37.1, Dec=+42:40:20) and Abell 963 ($z = 0.206$, RA=10:17:13.9, Dec=+39:01:31). The H I data allow us to sensitively probe the effects of galaxy transformation (e.g. ram-pressure stripping, starvation, harassment, and mergers) on atomic gas in galaxies in a range of environments. These two clusters were chosen for their contrasting dynamical states; A963 is extremely rich, X-ray luminous, and fairly dynamically relaxed, while A2192 is less massive, less X-ray luminous, and is less relaxed (Jaffé et al. 2013). Both clusters have been shown to contain significant substructure in our spectroscopic studies (Jaffé et al. 2013). All together, our study provides an unprecedented look at the evolutionary state of galaxies in a large dynamic range of environments, and at a redshift where the Butcher–Oemler effect (Butcher & Oemler 1984) first presents a strong increase in galaxy activity at high densities.

To fill in the missing pieces of the cold gas puzzle in these two clusters, we have begun a pilot study of the molecular gas content of BUDHIES galaxies with the Redshift Search Receiver (RSR) on the Large Millimeter Telescope *Alfonso Serrano* (LMT) in Mexico. Our pilot study, which we are calling CO Observations with the LMT of BUDHIES (COOL BUDHIES), has measured the CO emission line, or placed upper limits on the emission line, for a sample of 23 galaxies selected from the BUDHIES fields. Our sample, which is comprised of half H I-selected galaxies and half H I-undetected but selected via detections in the infrared with the Multiband Imaging Photometer for *Spitzer* (MIPS; Rieke et al. 2004), consists of targets with stellar masses $M_* \geq 10^{10}\ \mathrm{M_\odot}$ and spectroscopic redshifts from the optical and/or H I.

Section 2 describes our sample and our existing BUDHIES data (2.1), and our new LMT CO observations are described in Section 2.2. Section 2.2.1 describes our procedures for reduction and analysis of the new CO spectra, and in Section 2.2.2 we describe our accounting for false detections. In Section 2.3 we describe our primary reference sample, and in Section 3 we present our molecular gas masses (3.1), and compare the gas content of our target sample to our local reference sample. Section 3.2 compares the molecular and atomic gas masses in our sample, and to our reference sample, and Section 3.3 examines the gas content related to environment. We discuss the implications of our results, further interpretation, and highlight the next steps of the COOL BUDHIES project in Section 4. Throughout this paper we use cosmological parameters $\Omega_\Lambda = 0.70$, $\Omega_M = 0.30$, and $H_0 = 70\ \mathrm{km\,s^{-1}\,Mpc^{-1}}$, where pertinent cosmological quantities have been calculated using the online Cosmology Calculator of E. L. Wright (Wright 2006). We also assume a Kroupa IMF (Kroupa 2001).

2 SAMPLE AND DATA

2.1 BUDHIES sample

The foundation of the BUDHIES project is ultra-deep H I mapping with the Westerbork Synthesis Radio Telescope (WSRT), with

78×12 h on A2192 and 117×12 h on A963, to a 4σ detection threshold of $2 \times 10^9\,M_\odot$. The details of the H I observations, the data reduction, and catalogue generation can be found in Verheijen et al. (2007, 2010). Our WSRT survey revealed ∼160 H I detections spanning redshifts of $0.164 \leq z \leq 0.224$. To supplement these data we have obtained imaging with the *Galaxy Evolution Explorer* (*GALEX*; Martin et al. 2005) in NUV and FUV, *B* and *R* bands with the Isaac Newton Telescope (INT) on La Palma, United Kingdom Infrared Telescope (UKIRT) *J* (for A963), *H*, and *K* bands, and *Spitzer* Infrared Array Camera (IRAC; Fazio et al. 2004) and MIPS. To more fully sample the optical-to-NIR part of the spectrum, we also obtained data from the Sloan Digital Sky Survey (SDSS; York et al. 2000). For the SDSS, we generated mosaics in $u'g'r'i'z'$ with the online Montage Image Mosaic Service,[1] which produces science-grade mosaics by co-adding SDSS frames over an area of up to 1 deg². We also have spectroscopic redshifts for over 2000 galaxies in these two clusters, which come from a combination of spectra taken at the William Herschel Telesceope (WHT) in La Palma, the SDSS, the Wisconsin Indiana Yale NOAO Telescope, and MMT/Hectospec observations from Hwang et al. (2014), and from the Local Cluster Substructure Survey team (private communication). Details can be found in Jaffé et al. (2013) and in Jaffé et al. (2016).

The *Spitzer* IRAC and MIPS data (PI: A. Chung) were reduced using the IDL pipeline of R. Gutermuth (Gutermuth et al. 2009), and we use the MIPS [24] data to estimate the total infrared luminosity L_{IR} following the calibration of Rieke et al. (2009). The UKIRT near-IR data (PI: G. Morrison; JHK for A963 and HK for A2192) were processed by the JAC pipeline, and co-added mosaics were produced using the complementary Astromatic[2] tools SExtractor (Bertin & Arnouts 1996), SWarp (Bertin et al. 2002), and SCAMP (Bertin 2006). The *GALEX* FUV and NUV photometry (PI: J. H. van Gorkom) come from the reduced data products available from the Mikulski Archive for Space Telescopes[3] (MAST), which provides calibrated photometry catalogues for our maps of these two cluster fields.

Obtaining accurate stellar masses for our sample of galaxies can only be done with properly-calibrated photometry and band-merged catalogues. We de-redden the photometry using the foreground galactic extinction values from Schlegel, Finkbeiner & Davis (1998), assuming $R_V = 3.1$. The INT *R*-band image, being the deepest and highest resolution map of these clusters, forms the basis of our photometric catalogue. To make our band-merged catalogues, we first matched the astrometry of all our other images to the INT *R*-band frame, correcting for sub-arcsecond offsets that we measured using bright (but unsaturated) point sources detected using SExtractor in each frame. In the process of checking the astrometry, we found a common occurrence of a systematic offset in Declination of ∼0.3 arcsec for all of our frames compared to the INT *B*- and *R*-band frames, and so we adjusted the INT astrometry to be in better agreement with the median systematic offsets in Declination as well. After getting each frame on to a common astrometric solution, we measure photometry with SExtractor using Kron elliptical apertures for all bands from SDSS u' through IRAC [4.5]. We measure aperture corrections in each of these frames by comparing the elliptical-aperture photometry, for isolated sources, with the photometry measured from much larger circular apertures,

obtaining corrections of approximately 0.05–0.10 mag in each band. Finally, the individual catalogues are merged with the INT *R*-band source list to produce a final catalogue. The IRAC [5.8] and [8.0] photometry are excluded from our catalogues, as we found them to generally lack sufficient sensitivity. After merging the SDSS u' through IRAC [4.5] bands, we match the *GALEX* FUV and NUV catalogue as well as the MIPS [24] catalogue to the final band-merged catalogue.

After band-merging, we perform spectral energy distribution (SED) fitting using the Fortran-based code MAGPHYS[4] (da Cunha, Charlot & Elbaz 2008; da Cunha et al. 2015). SED fitting is restricted to only those galaxies having spectroscopic redshifts (either from optical or H I), keeping the redshift fixed and finding the best-fitting SED from the Bruzual & Charlot (2003) population synthesis models. The MAGPHYS code is built with a Bayesian framework, and it marginalizes over a number of parameters affecting the stellar light (e.g. metallicity and dust extinction) and it also can simultaneously find the best-fitting dust emission in the infrared, while maintaining energy balance between the absorbed UV-optical light and the re-emitted infrared (via polycyclic aromatic hydrocarbons in addition to warm and cold dust components). Since we are only concerned with the stellar component of the SED in our present analysis, and we only fit SEDs using the *GALEX* through IRAC [4.5], we ignore any of the dust information returned by MAGPHYS and use just the total stellar mass (converted to a Kroupa IMF). To estimate the typical 1σ dispersion of our stellar mass estimates, we exploit the fact that MAGPHYS returns a full probability distribution function (PDF) of the stellar mass. We stack on all of the stellar mass PDFs, centred on the maximum likelihood stellar mass of each, for all galaxies having a stellar mass $M_* \geq 10^{10}\,M_\odot$. The mean stacked PDF has a standard deviation of $\simeq 0.08$ dex, which we conservatively round up to 0.1 dex to help account for additional systematic uncertainties affecting our stellar mass estimates.

To verify that we have obtained reasonable mass estimates, we compare our stellar masses to those calculated using independent calibrations in the optical and near-to-mid-infrared. Our comparison optically derived stellar masses are from Zibetti, Charlot & Rix (2009), using our INT *B*- and *R*-band rest-frame photometry with:

$$\frac{M_*}{M_\odot} = L_R \times 10^{-1.200+1.066(\mathrm{mag}_B - \mathrm{mag}_R)} + 10^{0.04}, \qquad (1)$$

where L_R is the *R*-band luminosity (in $L_\odot$) and the $10^{0.04}$ term converts the IMF to Kroupa. Our other comparison stellar mass calibration comes from Eskew, Zaritsky & Meidt (2012) using IRAC [3.6] and [4.5]. We estimate stellar masses, similarly as we have in Cybulski et al. (2014), as

$$\log\left(\frac{M_*}{M_\odot}\right) = \log(0.69 \times 10^{5.65}) f_{I1}^{2.85} f_{I2}^{-1.85}(D_L/0.05)^2, \qquad (2)$$

where f_{I1} and f_{I2} are the rest-frame fluxes in [3.6] and [4.5], respectively, in Jy, D_L is the luminosity distance in Mpc, and the mass is also in a Kroupa IMF.

Using the ∼2000 galaxies in these two fields that have spectroscopic redshifts, detections in the optical and IRAC [3.6] and [4.5] bands, and a stellar mass range of $10^8 \leq M_* \leq 10^{12}\,M_\odot$, we compare the Zibetti et al. (2009) optical stellar masses and the Eskew et al. (2012) IRAC stellar masses to those of MAGPHYS. We find a strong linear correlation (with a Pearson correlation coefficient of 0.91 and 0.80 for the optical and IRAC stellar masses, respectively),
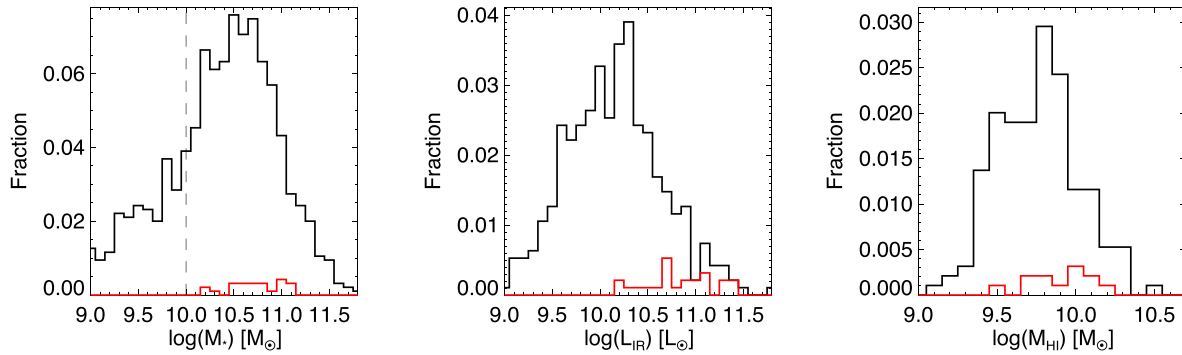
Figure 1. Histograms comparing the distribution of the parent sample of galaxies in the BUDHIES cluster fields (black) to the targets selected for this pilot study (red). The histograms have all been normalized by the total number of galaxies in the parent sample. The histograms show the distributions of stellar mass (left), infrared luminosity (middle), and H I mass (right). The vertical dashed line on the left-hand panel indicates the minimum stellar mass considered for this pilot study. The stellar masses shown here are derived using the MAGPHYS SED-fitting code (see Section 2.1 of the text).

a median stellar mass agreement of within 20 per cent, and a dispersion corresponding to 0.25 dex (for optical) and 0.32 dex (for IRAC). Hereafter, our stellar masses come from the MAGPHYS code.

Our targets were selected randomly from our band-merged catalogue from the galaxies satisfying the following criteria:

(i) $M_* \geq 10^{10} \, \mathrm{M_\odot}$,

(ii) spectroscopic redshifts, with $|z_{spec} - z_{cl}| \leq 0.05(1 + z_{cl})$, where z_{cl} is the redshift of the cluster,

(iii) either a detection in H I, or no detection in H I but a detection in MIPS [24].

The full sample of galaxies matching these selection criteria is over 150, but for the purposes of our pilot study we must restrict our observations to a small subset (see Figure 1). Therefore, our sample consists of roughly half galaxies that are H I selected, with no regard for their MIPS [24] flux, and half that are undetected in H I but are MIPS [24] selected. Note, however, that our redshift window for target selection for CO observations does not overlap exactly with the redshift window for our H I detections with the WSRT ($0.1646 \leq z_{HI} \leq 0.2241$). As a result, the 11 galaxies lacking H I data in our sample are comprised of six which are in the volume mapped by the WSRT, and have upper limits on their H I masses, and five which are outside of that volume (for which we have no data). Hereafter, we define galaxies as cluster members if they have projected separations of $R_{proj} \leq 3 \, R_{200}$ from the cluster centre and line-of-sight velocities within three times the velocity dispersion of the cluster.

2.2 New LMT observations

The LMT is a 50-m radio telescope located on Volcán Sierra Negra in Mexico, at an elevation of 4600 metres (Hughes et al. 2010). For the Early Science campaigns at the LMT, the inner 32.5 m of the primary dish is illuminated by the receiver optics. During the observing seasons, the median opacity at the site at 225 GHz is $\tau = 0.1$. The pointing RMS is 3 arcsec over the entire sky, but is reduced to 1–2 arcsec for targets located within ~10 deg of known sources.

We observed our targets with the RSR between 2014 March 13 and April 29 as part of the Early Science 2 (ES2) season at the LMT. The RSR has a novel design, with a monolithic microwave integrated circuit system, that receives signals over four pixels simultaneously covering a frequency range of 73–111 GHz, sampled at 31 MHz (corresponding to ~100 km s^{-1} at 90 GHz). The RSR has a beam full width half-maximum (FWHM) that is frequency

dependent, but for our targets it is $\simeq 23$ arcsec. The RSR beam FWHM is very well matched to the angular sizes of the optical discs of our target galaxies, whose median R_{90}, derived from our INT R-band mosaic, is 11.6 arcsec (see the postage-stamp images of our targets in Appendix A for a comparison of the optical discs to the RSR beam). The RSR system has been optimized to provide great stability in spectral baseline over the entire frequency range being sampled. The RSR was designed to operate on the LMT, but it has previously been commissioned on the Five College Radio Astronomy Observatory (FCRAO) 14-m telescope (e.g. Chung et al. 2009; Snell et al. 2011), and was also used recently with LMT observations in Kirkpatrick et al. (2014) and Zavala et al. (2015). For a technical description of the RSR system, see Erickson et al. (2007). Our observations were taken with a system temperature ranging from 87 to 113 K, and our targets were observed for about 1 h each (see Table 1 for specific integration times) with typical rms noise of ~0.190 mK.

2.2.1 Data reduction and analysis

We reduced the spectra using DREAMPY (Data REduction and Analysis Methods in PYTHON), a software package written by G. Narayanan specifically to reduce and analyse RSR spectra. The RSR produces four separate spectra for each observation; prior to co-adding them, the four spectra are individually calibrated and visually checked for any known instrumental artefacts that occasionally arise. Any portion of the spectrum found to exhibit those artefacts is flagged for removal.

After co-adding the spectra, we analyse them using a custom IDL code that fits the line with a Gaussian using a Markov Chain Monte Carlo (MCMC) approach to robustly determine the parameters of the line (amplitude, central frequency, standard deviation, and D.C. offset) and their statistical errors. We begin by searching for an initial Gaussian fit in the spectrum to a line having positive amplitude and a central frequency within ± 0.08 GHz of the expected CO frequency (corresponding to a velocity range of $\pm \sim 250$ km s^{-1}), based on the prior optical/H I redshift for each galaxy. Then we subtract off that best-fitting Gaussian from the spectrum and apply a Savitzky–Golay filter (Savitzky & Golay 1964) to the full spectrum that remains, to reduce the low-frequency signal. The Savitzky–Golay filter we use is a 'rolling' order-two polynomial fit to the spectrum with a width of 1 GHz. Note that the width of our Savitzky–Golay filter is significantly greater than the width of any astrophysical lines in our spectra. This filtering technique has been employed in many

Table 1. CO observations of our target galaxies, separated into members of the two clusters and foreground/background galaxies around the clusters. Column 2 gives the redshift of the target, based on prior optical or H I observations. Column 3 gives the integration time. Column 4 has the RMS of the RSR spectrum, measured over a frequency range of ± 1 GHz centred on the CO line (excluding the line itself). Column 5 has the integrated line flux, and Column 6 gives the central frequency of the CO line. Column 7 has the FWHM of the line, and Column 8 the redshift derived from the CO line. Note that we only give the latter of the derived quantities for the cases where we have a reliable detection (S/N ≥ 3.6)

Designation	$z_{opt/H\,i}$	t_{int} (h)	rms (mK)	$S_{CO}\Delta V$ (Jy km s^{-1})	ν_{CO} (GHz)	ΔV (km s^{-1})	z_{CO}
A2192 Galaxies							
J162523.6+422740	0.187	2.0	0.154	1.995 ± 0.294	97.1387 ± 0.0110	429 ± 52	$0.186\,67 \pm 0.000\,61$
J162644.6+422530	0.189	1.0	0.217	2.387 ± 0.293	96.9290 ± 0.0022	176 ± 12	$0.189\,23 \pm 0.000\,12$
J162528.4+424708	0.189	0.9	0.248	< 1.006	...	...	...
J162508.6+423400	0.190	1.0	0.218	1.326 ± 0.466	...	...	...
A2192 FG/BG Galaxies							
J162555.2+425747	0.134	1.0	0.246	4.708 ± 0.550	101.6751 ± 0.0128	598 ± 49	$0.133\,72 \pm 0.000\,94$
J162612.9+425242	0.146	1.0	0.196	3.329 ± 0.256	100.6082 ± 0.0019	161 ± 11	$0.145\,74 \pm 0.000\,13$
J162558.0+425320	0.169	1.9	0.175	< 0.856	...	...	...
J162710.8+422754	0.173	1.0	1.485	< 4.202	...	...	...
J162721.0+424951	0.220	2.1	0.137	0.949 ± 0.268	...	...	...
J162613.4+423304	0.224	1.0	0.216	< 0.637	...	...	...
J162717.7+430309	0.228	1.1	0.211	0.714 ± 0.294	...	...	...
J162830.3+425120	0.228	1.1	0.195	1.392 ± 0.386	93.7779 ± 0.0118	559 ± 150	$0.229\,19 \pm 0.000\,55$
A963 Galaxies							
J101703.5+384157	0.201	1.0	0.224	< 0.919	...	...	...
J101727.7+384628	0.201	1.2	0.230	0.852 ± 0.314	...	...	...
J101705.5+384925	0.204	1.0	0.237	< 1.537	...	...	...
J101540.2+384913	0.204	1.0	0.325	1.292 ± 0.445	...	...	...
J101730.0+385831	0.204	1.0	0.186	1.324 ± 0.313	95.7115 ± 0.0144	340 ± 50	$0.204\,36 \pm 0.000\,73$
J101803.6+384120	0.205	1.1	0.141	< 0.411	...	...	...
J101611.1+384924	0.207	1.0	0.208	1.640 ± 0.286	95.5613 ± 0.0075	203 ± 38	$0.206\,25 \pm 0.000\,38$
J101618.0+390613	0.208	1.0	0.253	1.771 ± 0.348	95.3854 ± 0.0052	198 ± 23	$0.208\,48 \pm 0.000\,26$
A963 FG/BG Galaxies							
J101856.7+390158	0.161	1.1	0.302	2.166 ± 0.690	...	...	...
J101712.2+390559	0.165	1.2	0.260	< 0.730	...	...	...
J101624.0+385840	0.169	2.0	0.163	2.146 ± 0.265	98.6013 ± 0.0067	319 ± 26	$0.169\,06 \pm 0.000\,40$

prior spectroscopic studies (e.g. Faran et al. 2014; Stroe et al. 2015; Wang et al. 2015). After computing the polynomial filter on the line-subtracted spectrum, we apply that filter to the original spectrum, and then we fit a final Gaussian to the CO emission line in the filtered spectrum. Our MCMC approach robustly samples the range of parameter space for our spectra near the expected frequency of the CO line, and we determine the 1σ errors on our CO line parameter estimates based on the posterior distribution found by our MCMC code. We run our MCMC line-fitting code for 4×10^4 steps as our initial 'burn-in', and then for 6×10^4 more steps to sample parameter space. Therefore, any ambiguity in the line properties that might arise due to low signal to noise is accounted for in our measurements. We include figures showing an example of our MCMC parameter fitting in Appendix B. A demonstration of the filtering applied to one of our spectra is shown in Fig. 2. In Fig. 3 we show the full spectrum of one of our targets, as well as a zoomed-in view of the portion of the spectrum near the identified CO line.

We convert the spectra from units of modified antenna temperature T_A^* to flux density by multiplying by the telescope gain of 7 Jy K^{-1} (F. P. Schloerb, private communication). And we also convert the spectra from units of frequency to velocity, centred on the ν_{CO} that we fit in the spectrum, and account for distortions when translating between frequency intervals and velocities at each galaxy's redshift following Gordon, Baars & Cocke (1992). Then we obtain the total line flux by integrating the spectrum over the velocity interval given by ± 2 times the standard deviation of the best-fitting Gaussian centred on the velocity of the line. The
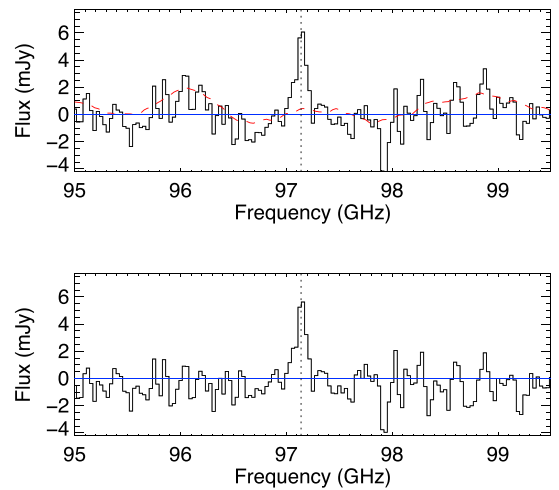

Figure 2. A portion of the spectrum of our target J162523.6+422740, centred on the CO line. The top panel shows the spectrum after reducing it with DREAMPY, without applying our Savitzky–Golay filter. The polynomial fit to the spectrum is denoted by the red dashed line. The bottom panel is the spectrum after filtering. The vertical dotted line in both panels shows the expected central frequency of the line, based on the prior redshift information.

associated error of the line flux measurement is determined by integrating the RMS measured in the spectrum over the same interval. Table 1 presents the basic results of the CO observations, including the integrated line fluxes, FWHM, and derived
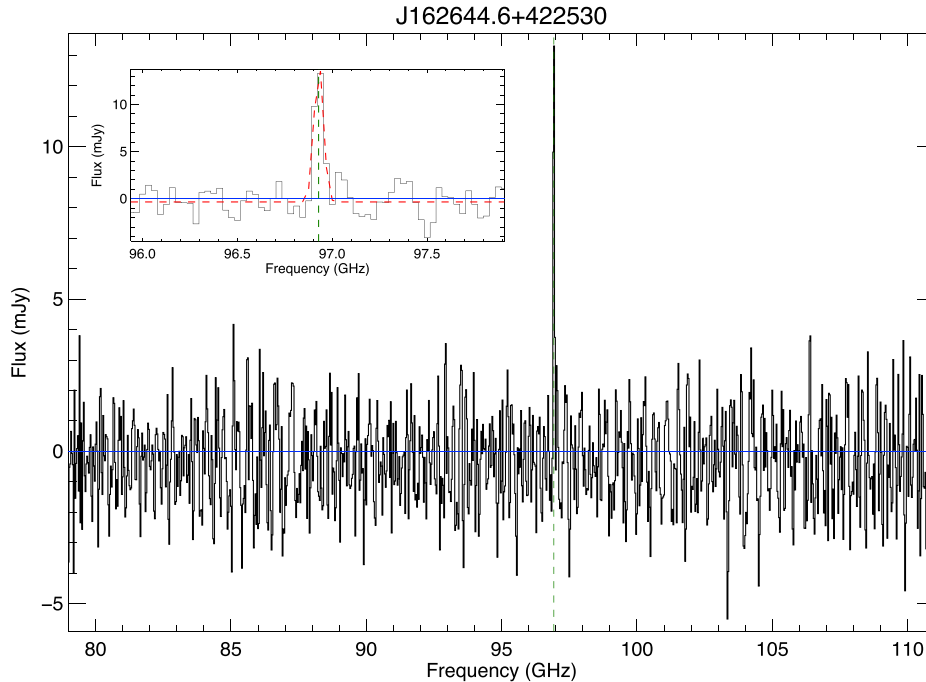
Figure 3. CO spectrum of one of our targets (J162644.6+422530), after filtering, with a strong detection of the $^{12}CO\,J = 1 \rightarrow 0$ transition line. The vertical dashed green line indicates the frequency where we expect to detect the line, based on the H I redshift. The full spectrum is seen in the main figure and a zoomed-in view, centred on the frequency of the CO line, is in the inset. The dashed red line in the inset denotes the Gaussian fit to the CO line.

CO redshifts. Appendix A presents all of our CO spectra, along with optical postage stamp images and the H I spectrum, of our target galaxies.

2.2.2 False detection rate

Given that our technique for identifying molecular emission lines assumes a narrow range in central frequency, based on prior redshift information, and then searches for the best-fitting Gaussian near that frequency, we want to be sure that we understand the statistical significance of our detections and signal-to-noise measurements. To explore this more rigorously, we performed a set of random trials to test the likelihood of false detections in our spectra.

We select 2000 random combinations of frequency and target number. Therefore, we select, on average, about 90 random frequencies per spectrum, while avoiding the parts of our spectra where we know or expect a CO line to be located. Then we run our filtering and line detection algorithm on each of our random selections, which presumably only consist of noise, recording any instance of a 'detection' and its signal to noise. Next, we use the cumulative distribution of the signal-to-noise values recovered in these random trials to determine at which of our measured signal-to-noise values do we truly find the standard deviation. Fig. 4 shows the results of our false detection tests. $S/N_{1\sigma}$ corresponds to the signal to noise where our cumulative distribution reaches 68.269 per cent, and $S/N_{2\sigma}$ is when the cumulative distribution hits 95.45 per cent. These tests reveal that $S/N_{1\sigma} = 1.8$, and $S/N_{2\sigma} = 3.6$, as shown in Fig. 4, and they imply that we could expect a false detection rate of between 5 and 25 per cent for detections of $2.0 < S/N < 3.6$, and a false detection rate of less than 5 per cent for an $S/N \geq 3.6$. Based on these tests, we decide to count any detections with $2.0 < S/N < 3.6$ as 'marginal' and only consider an $S/N \geq 3.6$ to be a reliable detection. We do consider the integrated line flux, and estimated
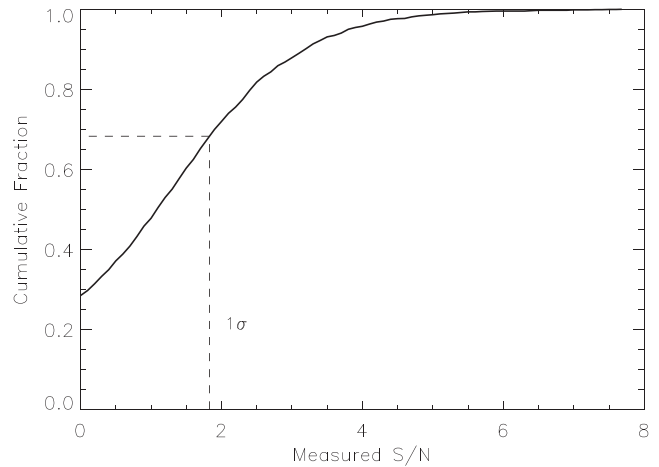

Figure 4. Cumulative distribution of signal-to-noise measured using our MCMC code for 2000 randomly selected frequencies in our RSR spectra (avoiding parts of the spectrum where we expect a CO line). The dashed line indicates the signal-to-noise values corresponding to 1 times the standard deviation.

molecular gas mass, for marginal detections, but we do not derive any other parameters (e.g. CO redshifts) for them.

2.3 Reference sample: COLD GASS

For any pilot study such as ours, it is extremely important to place our results into context with previous studies that have examined similar astrophysical quantities. The natural choice for a reference sample to our current study is the COLD GASS (Saintonge et al. 2011). COLD GASS is an IRAM 30-m legacy survey that targeted about 350 nearby ($z \leq 0.05$) galaxies with stellar masses $M_* \geq 10^{10}\,M_\odot$. The COLD GASS sample is mass selected from

the parent GASS survey (Catinella et al. 2010), which consists of H I observations with Arecibo for nearby massive galaxies selected from the SDSS and *GALEX*. We obtained the COLD GASS data products from their third public data release on their project website.[5] The COLD GASS data set has also been used as a reference sample in Jablonka et al. (2013) and in Lee et al. (2014).

To provide a better comparison with our own study, we supplement the available data products for COLD GASS with photometry from the *Wide-Field Infrared Survey Explorer* (*WISE*; Wright et al. 2010), which has mapped the whole sky in 3.4, 4.6, 12, and 22 μm. As in Cybulski et al. (2014), we found matches to *WISE* by searching in the AllWISE catalogue (Mainzer et al. 2011) for counterparts within a 5 arcsec search radius centred on the SDSS galaxy positions of the COLD GASS sample galaxies. We use the *WISE* [22] photometry to estimate L_{IR} and SFR$_{IR}$, also using the calibration of Rieke et al. (2009).

2.3.1 Aperture corrections and beam contamination

One key benefit of our targets being at higher redshift than those of the COLD GASS sample is that the beam for our CO observations more completely covers the discs of our galaxies than for our lower z reference sample. Consequently, we can confidently measure the full extent of the CO emission in our targets without concern for missing any appreciable flux. Saintonge et al. (2011) showed that for the COLD GASS sample, with a beam approximately the same size as that of the RSR (22 arcsec), they require a range of aperture corrections for their CO fluxes from ∼20–50 per cent, depending on the angular size of the galaxy. If we apply their aperture correction formula to our targets, using the measured optical sizes of our targets, we would require corrections of less than 2 per cent. Given that our measurement uncertainties are significantly greater than this correction factor, we opt not to apply these aperture corrections for our sample. The COLD GASS catalogues that we compare our sample with had aperture corrections applied to their CO measurements. For a comparison of the angular sizes of our targets in contrast with those of the COLD GASS sample, see the figures in Appendix C.

However, a potential drawback of the relative size of our aperture being greater, compared to the angular extent of our target galaxies, is the risk of contamination from nearby galaxies in our beam. This is a particularly significant concern when observing targets in crowded fields, like in galaxy clusters such as ours. Note, however, that beam contamination is only an issue when we have additional galaxies within the RSR beam whose redshifts are the same. Although we occasionally find additional optical detections in our maps within the RSR beam, we do not typically encounter multiple targets that are bright in the infrared and overlapping with our beam. And even when we do, the redshifts of the contaminating sources generally do not coincide with the target redshifts (the one exception is J162721.0+424951, although in that case the dominant source of the infrared emission is our primary RSR target). Given that the strength of the CO line correlates strongly with infrared emission (see Fig. 5), we use our *Spitzer* MIPS data to assess possible CO contamination, and also to correct for it when we have sources with co-incident redshifts and positions within the target RSR beam.

3 RESULTS

3.1 CO luminosities and molecular gas masses

We calculate the CO line luminosity by

$$\frac{L'_{CO}}{K\ km\ s^{-1}\ pc^2} = 3.25 \times 10^7 S_{CO} \Delta V \nu_{obs}^{-2} D_L^2 (1+z)^{-3}, \quad (3)$$

following Solomon & Vanden Bout (2005), where ν_{obs} is the frequency of the line in GHz and D_L is the luminosity distance in Mpc. In Fig. 5, we plot the infrared luminosities versus CO line luminosities for our target sample, compared to similar observations gathered from the literature (Scoville et al. 2003; Gao & Solomon 2004; Chung et al. 2009; Geach et al. 2009, 2011; Jablonka et al. 2013; Kirkpatrick et al. 2014). Our galaxies that are detected in CO follow the established trends in the literature, and they mostly occupy an intermediate space between the less-infrared-luminous galaxies of COLD GASS and the ultra-luminous infrared galaxies (ULIRGs) from Chung et al. (2009). Furthermore, in Fig. 5 we see no apparent difference between the cluster members and the foreground/background galaxies in our sample.

To obtain estimates of molecular gas masses, we assume a CO-to-H$_2$ conversion factor of $\alpha_{CO} = 4.6\ M_\odot (K\ km\ s^{-1}\ pc^2)^{-1}$, which is roughly the value observed in the Milky Way (Bolatto, Wolfire & Leroy 2013), and implies the following conversion:

$$\frac{M_{H_2}}{M_\odot} = \frac{4.6 L'_{CO}}{K\ km\ s^{-1}\ pc^2}. \quad (4)$$

Table 2 gives the resulting CO line luminosities, infrared luminosities, and baryonic mass components (molecular gas, atomic gas, and stellar) for the galaxies in our sample. It is worthwhile to note that we unfortunately have only one galaxy in our sample that is not a cluster member and has detections in both molecular and atomic gas. This is partly due to small number statistics, but it is also a consequence of the target selection window in redshift space ($|z_{spec} - z_{cl}| \leq 0.05(1 + z_{cl})$) being a bit wider than the redshift window over which our WSRT mapping can detect galaxies in H I ($0.1646 \leq z_{HI} \leq 0.2241$), as first mentioned in Section 2. When we lack an H I detection due to a non-detection in the H I mapping, we indicate the upper limit on the H I gas mass in Table 2. However, when we lack an H I detection because the target is outside of the redshift range of the H I spectrum, we denote the H I gas mass with '...' in Table 2 and we exclude these targets from any figures involving H I gas mass hereafter.

3.2 Molecular versus atomic gas masses

In Fig. 6, we plot a comparison of the molecular and atomic gas masses, normalized by stellar mass, between our targets and the COLD GASS sample. Note that the COLD GASS catalogs have molecular gas masses derived with a α_{CO} of 4.35 (and 1.0 for the most infrared luminous galaxies), unlike our 4.6. In our comparisons, we have re-scaled the COLD GASS galaxies to match our adopted α_{CO} factor throughout this work. It is notable that our detections in CO show molecular gas masses generally in excess of most of the COLD GASS sample, while our atomic gas masses show no such excess. However, given that our selection of targets is based in part on L_{IR}, and that our threshold for detecting molecular gas is higher than with the COLD GASS sample, it is not surprising that our sample would produce molecular gas detections that are high relative to what is observed in the more local, not infrared-selected, sample of COLD GASS galaxies. Nevertheless, it is interesting that
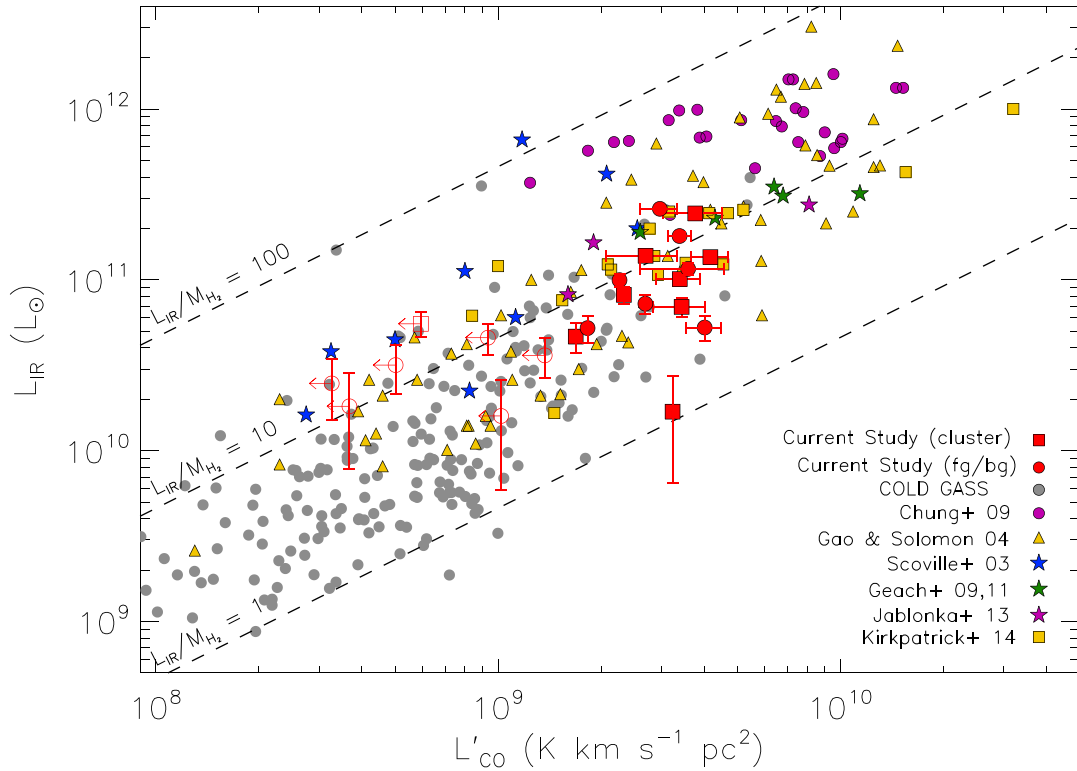
Figure 5. Infrared luminosity versus CO line luminosity for our current sample (red squares are cluster members, and red circles are targets in the foreground or background of our clusters). Open red squares and circles indicate non-detections. The dashed lines indicate constant values of the ratio of L_{IR} to M_{H_2} (both in solar units). We also compare our sample to a number of other studies collected in the literature. The grey circles are galaxies from COLD GASS (Saintonge et al. 2011) with detections in CO and *WISE* [22]. The purple circles are nearby ULIRGs from Chung et al. (2009), observed with the RSR on the FCRAO 14-m telescope. Yellow triangles correspond to the sample of Gao & Solomon (2004). Blue stars are low-redshift QSOs from Scoville et al. (2003), and the green and blue squares indicate the intermediate-redshift cluster galaxies from Geach et al. (2009, 2011) and Jablonka et al. (2013). The yellow squares are from Kirkpatrick et al. (2014). Note that the infrared luminosities being plotted for the Kirkpatrick et al. (2014) points are not corrected to remove the contribution due to an active galactic nucleus, to remain consistent with the rest of the data being plotted.

those same galaxies with high molecular gas masses, relative to the local reference sample, generally appear to have atomic gas masses that are more typical of the reference sample.

We further examine the differences in the relative quantities of atomic and molecular gas between our sample and COLD GASS by comparing their baryonic fractions of the two gas components, and of the fraction of their total cold gas. We calculate the fractions of molecular and atomic gas as

$$f_{H_2} = M_{H_2}/(M_{H_2} + M_{Hi} + M_*) \qquad (5)$$

$$f_{Hi} = M_{Hi}/(M_{H_2} + M_{Hi} + M_*), \qquad (6)$$

and present the gas mass fractions in Fig. 7. The fraction of cold gas is calculated as follows,

$$f_{gas} = (M_{H_2} + M_{Hi})/(M_{H_2} + M_{Hi} + M_*). \qquad (7)$$

We also find that the molecular gas fractions for our targets are in excess of the majority of the COLD GASS sample, with 10–40 per cent molecular gas fractions for our targets that have detections in both gas components. As before, we also find that the H I gas fractions for our sample are typical of the atomic gas fractions for the reference sample, given their stellar masses. For the six galaxies having detections in both cold gas components, we measure an overall cold gas fraction f_{gas} (in the right-hand panel of Fig. 7) of 20–40 per cent, which is somewhat gas rich compared to the rest of the COLD GASS sample but not as much of an excess as when we

compare the molecular gas abundances alone. While the panels of Fig. 7 show how the relative fractions of molecular and atomic gas components compare for the two samples, they do not show a direct comparison between the molecular and atomic gas masses for these samples.

A direct comparison between the molecular and atomic gas masses for the two samples is shown in Fig. 8. Here we find the differences in molecular-to-atomic gas between our sample and the COLD GASS reference galaxies the most apparent. The galaxies detected in both CO and H I in our survey all lie on or above the 1:1 line in Fig. 8, whereas the vast majority of the COLD GASS galaxies are on the H I-dominated side. However, when we highlight the more infrared luminous galaxies in the COLD GASS sample, the ∼15 per cent with $L_{IR} \geq 10^{9.5}$ L$_\odot$, in Fig. 8, we do see that the infrared-selected subset does include most of the galaxies that are more molecular gas rich in the COLD GASS sample.

3.3 Molecular gas and environment

Our sample for this pilot study is split between cluster members (12) and non-members (11) with the intention that we might explore, in a very basic way, the differences we see between the half of our sample located in clusters to the half outside of the clusters. The general statistics for cluster members versus non-members are presented in Table 3. With such small numbers, it is difficult to draw any significant conclusion from a comparison of the cluster members

Table 2. Relevant luminosities and masses for our target galaxies. Column 2 gives the molecular gas line luminosity. Columns 3, 4, and 5 give the molecular gas, atomic gas, and stellar mass, respectively. Column 6 shows the infrared luminosity.

Designation	L'_{CO} (10^9 K km s^{-1} pc^2)	M_{H_2} (10^9 M$_\odot$)	M_{HI} (10^9 M$_\odot$)	M_* (10^{10} M$_\odot$)	$\log(L_{IR})$ (L$_\odot$)
A2192 Galaxies					
J162523.6+422740	3.40 ± 0.50	15.62 ± 2.30	<2.00	1.77	11.00
J162644.6+422530	4.17 ± 0.51	19.18 ± 2.36	6.36 ± 0.53	6.00	11.13
J162528.4+424708	<1.75	<8.07	9.70 ± 0.46	1.49	10.74
J162508.6+423400	2.33 ± 0.82	10.72 ± 3.76	<2.00	10.05	10.91
A2192 FG/BG Galaxies					
J162555.2+425747	4.01 ± 0.47	18.46 ± 2.16	...	3.75	10.72
J162612.9+425242	3.39 ± 0.26	15.59 ± 1.20	...	12.96	11.26
J162558.0+425320	<1.18	<5.43	11.36 ± 0.71	3.16	10.39
J162710.8+422754	<6.06	<27.88	6.53 ± 0.46	4.50	10.20
J162721.0+424951	2.26 ± 0.64	10.41 ± 2.95	4.70 ± 0.45	4.29	11.00
J162613.4+423304	<1.58	<7.25	5.23 ± 0.49	1.81	10.50
J162717.7+430309	1.83 ± 0.75	8.40 ± 3.46	...	2.93	10.72
J162830.3+425120	3.59 ± 0.99	16.51 ± 4.58	...	10.48	11.06
A963 Galaxies					
J101703.5+384157	<1.82	<8.37	<2.00	4.92	10.66
J101727.7+384628	1.69 ± 0.62	7.75 ± 2.86	10.00 ± 0.68	7.25	10.67
J101705.5+384925	<3.13	<14.41	8.44 ± 0.59	4.37	10.56
J101540.2+384913	2.62 ± 0.90	12.05 ± 4.15	9.34 ± 0.58	5.09	10.23
J101730.0+385831	2.70 ± 0.64	12.41 ± 2.93	3.51 ± 0.26	2.95	11.14
J101803.6+384120	<0.85	<3.91	16.80 ± 0.96	9.40	10.26
J101611.1+384924	3.44 ± 0.60	15.81 ± 2.75	13.54 ± 0.76	11.81	10.84
J101618.0+390613	3.77 ± 0.74	17.32 ± 3.41	<2.00	6.37	11.39
A963 FG/BG Galaxies					
J101856.7+390158	2.69 ± 0.86	12.39 ± 3.95	...	12.23	10.86
J101712.2+390559	<0.95	<4.39	<2.00	5.88	11.28
J101624.0+385840	2.97 ± 0.37	13.66 ± 1.69	<2.00	9.73	11.42
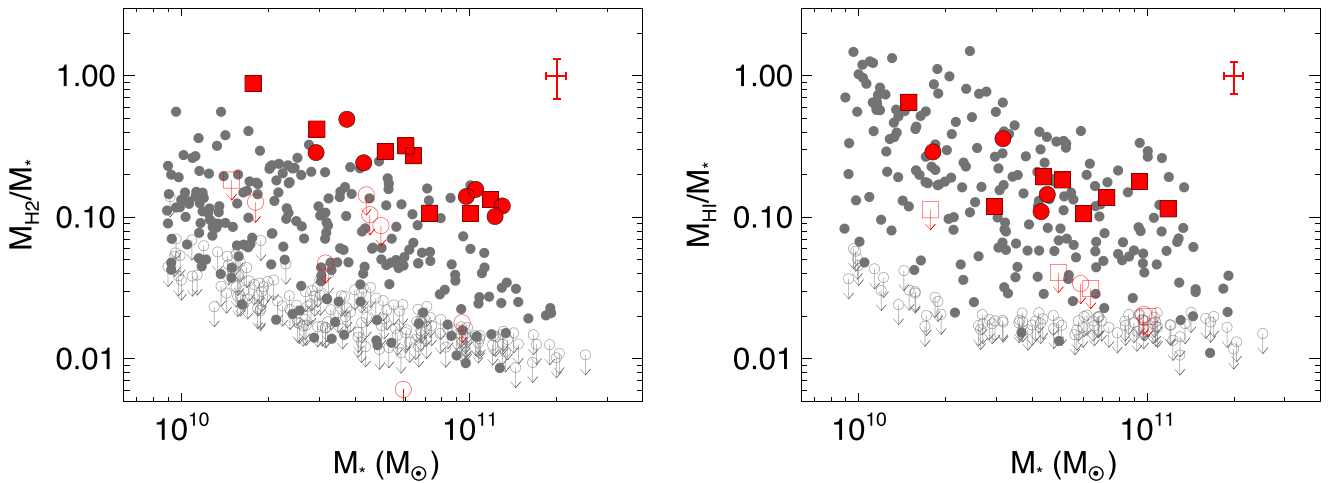
Figure 6. Left: molecular gas masses, normalized by stellar mass, versus stellar mass for our target sample (in red) compared with the COLD GASS sample (grey). As in Fig. 5, cluster members are squares and fg/bg galaxies are circles. Open symbols indicate non-detections. Right: atomic gas masses, normalized by stellar mass, versus stellar mass for our target sample (in red) compared with the COLD GASS sample (grey).

versus the non-members, apart from the fact that the molecular gas detection rates seem to have no strong dependence on whether the galaxies are in a cluster or not. Indeed, in Figs 6 and 7 the distribution of cluster members (denoted by red squares) is indistinguishable from that of non-members (red circles).

A meaningful examination of the role of environment requires a more complete sampling of the cluster environment than what we can accomplish with such a small target list. Our cluster members include just one galaxy (J101730.0+385831) having a projected radius within the virial radius of its parent cluster, although it is

worth noting that this particular galaxy is detected in CO. Of the remaining cluster members, seven have projected radii of between 1 and 2 times the virial radius, and four are projected at more than 2 times the virial radius. There is no obvious correlation between projected radius and CO content that we can discern from this sample. A follow-up to this pilot study has already been carried out in the LMT Early Science 3 (ES3) phase that addresses this limitation of the pilot study, and will be presented in Cybulski et al. (in preparation). More details of this follow-up study are described in the discussion at the end of Section 4.
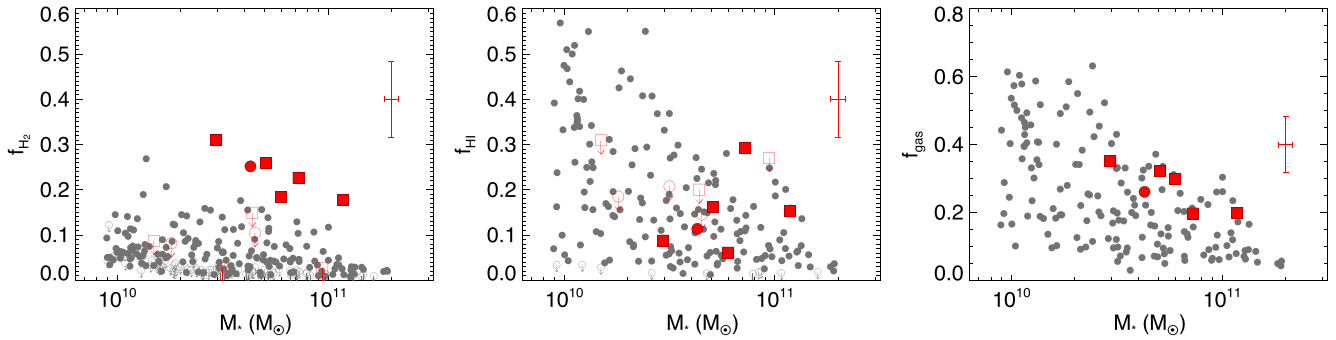
Figure 7. Left: molecular gas fraction versus stellar mass for our target sample (red) compared to the COLD GASS sample (grey), where the molecular gas fraction takes into account the atomic, molecular, and stellar component (see equation 5). Middle: atomic gas fraction versus stellar mass for our target sample (red) compared with the COLD GASS sample (grey), where the atomic gas fraction takes into account the atomic, molecular, and stellar component (see equation 6). Right: total cold gas fraction versus stellar mass, where we now include only those galaxies in our sample (red) and in the COLD GASS sample (grey) that are detected in both H I and CO (see equation 7). As in previous figures, open red symbols indicate non-detections.
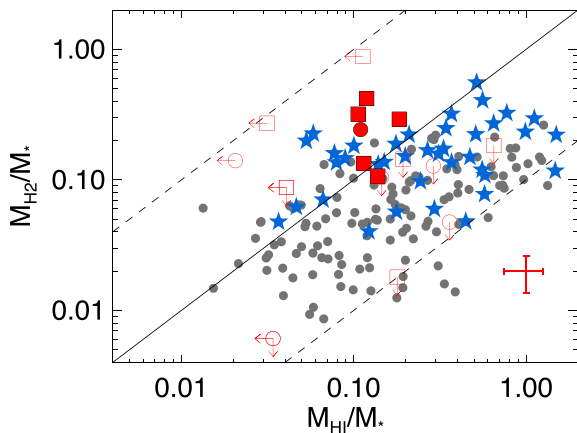
Figure 8. Molecular gas mass versus atomic gas mass, both normalized by stellar mass, for our sample (red) compared to the COLD GASS sample. The blue stars indicate galaxies in the COLD GASS sample with $L_{IR} \geq 10^{9.5} L_{\odot}$, and the grey circles are galaxies in COLD GASS with $L_{IR} < 10^{9.5} L_{\odot}$. The solid line indicates a 1:1 ratio of molecular-to-atomic gas mass, while the upper and lower dashed lines indicate a 10:1 and 1:10 ratio of molecular-to-atomic gas mass, respectively.

Table 3. Basic statistics on the cluster members and non-members in our sample, including the number of detections of CO , and the mean signal to noise of those detections.

	# Total	# Detections (S/N>2.0)	# Reliable detections (S/N>3.6)	⟨S/N ⟩ (detections)
Cluster Memb.	12	8	5	4.9
Cluster Non-memb.	11	7	4	6.1

4 CONCLUSIONS AND DISCUSSION

We have completed a pilot CO study, COOL BUDHIES, targeting a sample of galaxies in and around $z \sim 0.2$ clusters using the RSR on the new LMT. Our sample consists of about half galaxies that are H I selected, and half which lack H I detections but are selected based on MIPS [24]. Out of 23 galaxies in our sample, we reliably detect the $^{12}CO\, J = 1 \rightarrow 0$ emission line (with S/N ≥ 3.6) in nine galaxies, and we derive FWHM and CO redshifts for those galaxies. We also find marginal detections (with $2.0 < S/N < 3.6$) for six galaxies, which we treat differently from the non-detections

because we find the emission line in the spectrum co-incident with the expected frequency based on their prior redshift information. For the remaining eight galaxies in our sample we fail to detect the CO line with even a marginal statistical significance in ∼1 h of integration.

There is an obvious correlation between infrared luminosity and the quantity of molecular gas, consistent with previous studies (Young & Scoville 1991). Eight out of the nine LIRGs in our sample (89 per cent) are detected in CO, while only seven out of the 14 galaxies below the LIRG threshold in infrared luminosity (50 per cent) have molecular gas detections. We also find our most molecular gas-rich systems to typically be the most infrared luminous, as the subset of our targets having $M_{H_2} \geq 10^{10}\,M_{\odot}$ includes all but one of the LIRGs.

We find a strong tendency for our target sample to be more molecular gas dominated than the reference sample. While there are several possible factors that could contribute to this tendency, the most significant factor is a bias introduced by our target selection (driven by the infrared selection of half of the sample) and by Eddington bias. We can rule out the influence of the cluster environment (e.g. ram-pressure stripping) as a significant cause, as we see no difference between the distribution of cluster members and foreground and background galaxies in Figs 6 and 7. It is abundantly clear, however, that we need improved statistics and a more complete sampling of the cluster environment to assess any affect that the environment has on the gas content of the cluster members.

One other potential cause of the molecular gas abundance of our sample that is worth exploring is the redshift evolution in the molecular gas fraction from $z \sim 0$ to $z \sim 0.2$. Recent work by Genzel et al. (2015), combining new molecular gas measurements with work from the literature, indicates that one should expect to find approximately a 30 per cent increase in the molecular gas fraction for galaxies on the 'star-forming main sequence' between the redshift of the COLD GASS sample and the BUDHIES clusters. Similarly, Geach et al. (2011) proposed that the molecular gas fraction evolves as $\propto (1 + z)^{2 \pm 0.5}$, which implies an increase in the molecular gas fraction of ∼30 ± 8 per cent for a similar sample of galaxies between the redshift of our comparison sample and the sample in our pilot study. To examine this further, we have compiled data from various sources in the literature, consisting of molecular gas masses and stellar masses, spanning a wide redshift range to place this study in the context of our current picture of the evolution of molecular gas abundance in galaxies. We show this molecular gas abundance comparison in Fig. 9, along with the approximate
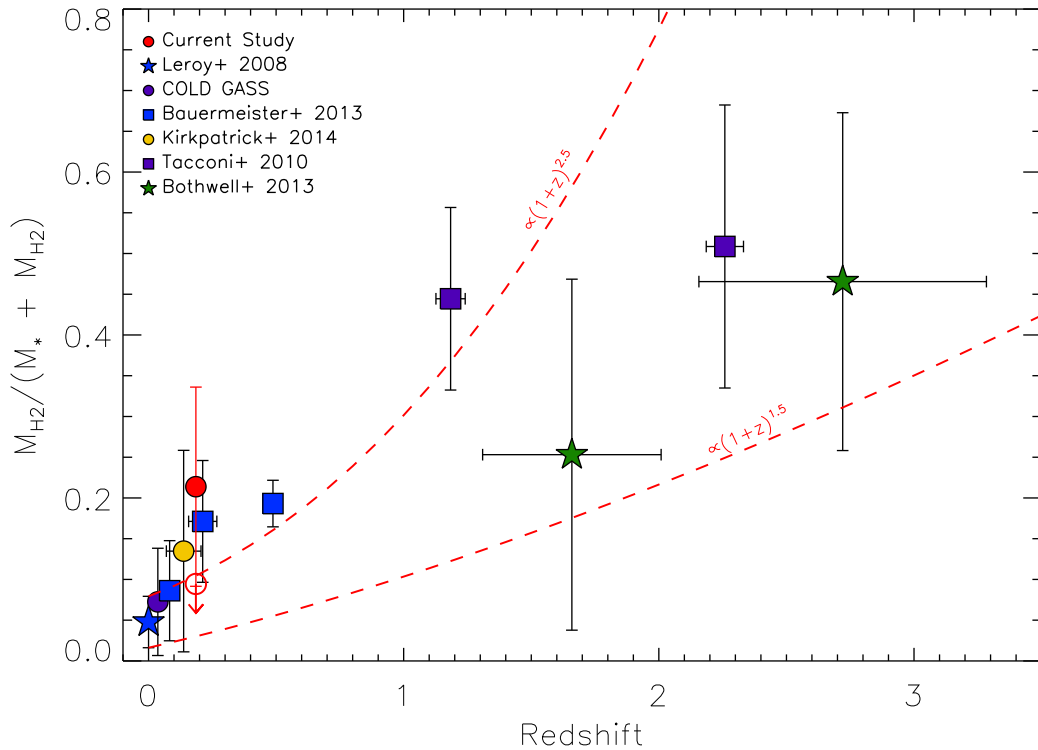
Figure 9. Molecular gas fraction (ignoring atomic hydrogen) as a function of redshift. The median molecular gas fraction for the galaxies with CO detections in our current study are plotted with the red filled circle. The open red circle indicates the median upper limit on the molecular gas fraction from our non-detections. Also plotted are the range of molecular gas fractions from Leroy et al. (2008, blue star), Saintonge et al. (2011, purple circle), Bauermeister et al. (2013, blue squares), Kirkpatrick et al. (2014, yellow circle), Tacconi et al. (2010, purple squares), and Bothwell et al. (2013, green stars). The red dashed lines show the approximate upper and lower limits for the proposed redshift evolution of the molecular gas fraction from Geach et al. (2011). Note that the molecular gas fractions for our detections lie about 1σ above the upper boundary of the proposed trend, but that the median upper limit for our whole sample, including the non-detections, lies within the expected range of molecular gas abundance.

upper and lower boundaries of expected evolution based on the proportionality of Geach et al. (2011). One important caveat of Fig. 9 is that these various studies comprise a highly heterogeneous sample of galaxies, and differences intrinsic to the particular Hubble types, star formation and gas accretion histories, environments, and ISM properties of the galaxies being sampled could all affect the abundance of molecular gas in these studies. Nevertheless, it is still relevant to place our results in context with other studies, as it can help highlight how or why our sample differs with those studies. It is clear from our comparison in Fig. 9 that the relative abundance of molecular gas that we find in our study is not accounted for in terms of the expected redshift evolution alone, as our detections (filled red circle) lie approximately 1σ above the expected redshift evolution. Furthermore, when we calculate an upper limit on the molecular gas abundance that includes our non-detections (open red circle) it lies well within the expected trend with redshift.

Therefore, we are left with the clear indication that the apparent overabundance of molecular gas in our pilot study is due to target selection and Eddington bias. About half of our sample (those lacking H I detections) are selected in the infrared, and that selection process will inherently result in a greater fraction of galaxies rich in molecular gas. This tendency can also be seen in Fig. 1, which shows that our targets tend to be skewed towards greater infrared luminosity than the parent sample (centre panel), whereas the atomic gas masses do not show an obvious difference between the parent sample and our pilot study's sub-sample (right-hand panel). Additionally, the apparent high abundance of molecular gas in the targets of our study could be driven by Eddington bias, as our limits of CO detection are not as low as in the COLD GASS study.

Therefore, we only have reliable detections of molecular gas for the 'upper envelope' of the most molecular gas-rich subset of galaxies we have targeted (e.g. our detections are on the upper boundaries of the distribution of our comparison sample in the left-hand panels of Figs 6 and 7).

One of the primary goals of the BUDHIES project is to understand the evolution of cold gas in galaxies out to intermediate redshifts, and in particular to study the effects (if any) of the cluster environment on that evolution. For our pilot COOL BUDHIES study, we have only a limited sample of targets to examine. Nevertheless, by choosing our sample strategically we have found some insight into the effects of target selection that will benefit our future study. From this study we have confirmed that infrared luminosity is an extremely effective predictor of molecular gas abundance, while H I has little-to-no relation with H_2 for our sample at $z \sim 0.2$. Our follow-up study, which has already been carried out in the LMT ES3 season, has targeted an additional 43 galaxies in the cluster A963. The expanded study includes targets that populate different parts of projected phase space and a range of galaxy colours. Our combined ES2 and ES3 spectra will include 50 galaxies populating the dynamical space around the massive cluster A963, and all having a range of H I masses and infrared luminosities. With these data we will more sensitively probe the effects of the cluster environment on molecular gas, as even with non-detections (which we anticipate for redder, less infrared-luminous galaxies) we will have sufficient statistics to stack on our CO spectra to examine the average molecular gas content of galaxies as a function of stellar mass, colour, infrared luminosity, and environment. Furthermore, a side-by-side comparison to stacks of H I spectra for our galaxies

will provide a much more statistically robust examination of the effects of environment on the atomic and molecular component of the ISM. The observations have been completed for the follow-up ES3 study, and reductions of the spectra are finished. The results will be presented in a forthcoming paper.

REFERENCES

Aravena M. et al., 2012, MNRAS, 426, 258
Bauermeister A. et al., 2013, ApJ, 768, 132
Bertin E., 2006, in Gabriel C., Arviset C., Ponz D., Enrique S., eds, ASP Conf. Ser. Vol. 351, Astronomical Data Analysis Software and Systems XV. Astron. Soc. Pac., San Francisco, p. 112
Bertin E., Arnouts S., 1996, A&AS, 117, 393
Bertin E., Mellier Y., Radovich M., Missonnier G., Didelon P., Morin B., 2002, in Bohlender D. A., Durand D., Handley T. H., eds, ASP Conf. Ser. Vol. 281, Astronomical Data Analysis Software and Systems XI. Astron. Soc. Pac., San Francisco, p. 228
Bolatto A. D., Wolfire M., Leroy A. K., 2013, ARA&A, 51, 207
Boselli A., Gavazzi G., Lequeux J., Buat V., Casoli F., Dickey J., Donas J., 1997, A&A, 327, 522
Boselli A., Cortese L., Boquien M., Boissier S., Catinella B., Gavazzi G., Lagos C., Saintonge A., 2014, A&A, 564, A67
Bothwell M. S. et al., 2013, MNRAS, 429, 3047
Bruzual G., Charlot S., 2003, MNRAS, 344, 1000
Butcher H., Oemler A., Jr, 1984, ApJ, 285, 426
Carilli C. L., Walter F., 2013, ARA&A, 51, 105
Casoli F., Dickey J., Kazes I., Boselli A., Gavazzi P., Baumgardt K., 1996, A&A, 309, 43
Catinella B., Cortese L., 2015, MNRAS, 446, 3526
Catinella B., Haynes M. P., Giovanelli R., Gardner J. P., Connolly A. J., 2008, ApJ, 685, L13
Catinella B. et al., 2010, MNRAS, 403, 683
Catinella B. et al., 2012, A&A, 544, A65
Catinella B. et al., 2013, MNRAS, 436, 34
Chung A., Narayanan G., Yun M. S., Heyer M., Erickson N. R., 2009, AJ, 138, 858
Combes F., García-Burillo S., Braine J., Schinnerer E., Walter F., Colina L., 2013, A&A, 550, A41
Cybulski R., Yun M. S., Fazio G. G., Gutermuth R. A., 2014, MNRAS, 439, 3564
da Cunha E., Charlot S., Elbaz D., 2008, MNRAS, 388, 1595
da Cunha E. et al., 2015, ApJ, 806, 110
Daddi E. et al., 2010, ApJ, 713, 686
Davé R., Finlator K., Oppenheimer B. D., 2012, MNRAS, 421, 98
Davé R., Katz N., Oppenheimer B. D., Kollmeier J. A., Weinberg D. H., 2013, MNRAS, 434, 2645
Dressler A., 1980, ApJ, 236, 351
Erickson N., Narayanan G., Goeller R., Grosslein R., 2007, in Baker A. J., Glenn J., Harris A. I., Mangum J. G., Yun M. S., eds, ASP Conf. Ser. Vol. 375, From Z-Machines to ALMA: (Sub)Millimeter Spectroscopy of Galaxies. Astron. Soc. Pac., San Francisco, p. 71
Eskew M., Zaritsky D., Meidt S., 2012, AJ, 143, 139
Fabello S., Catinella B., Giovanelli R., Kauffmann G., Haynes M. P., Heckman T. M., Schiminovich D., 2011, MNRAS, 411, 993
Faran T. et al., 2014, MNRAS, 442, 844
Fazio G. G. et al., 2004, ApJS, 154, 10
Fernández X. et al., 2013, ApJ, 770, L29
Gallazzi A. et al., 2009, ApJ, 690, 1883
Gao Y., Solomon P. M., 2004, ApJ, 606, 271
Gavazzi G., 1987, ApJ, 320, 96
Gavazzi G., O'Neil K., Boselli A., van Driel W., 2006, A&A, 449, 929
Gavazzi G., Fumagalli M., Cucciati O., Boselli A., 2010, A&A, 517, A73
Geach J. E., Smail I., Coppin K., Moran S. M., Edge A. C., Ellis R. S., 2009, MNRAS, 395, L62
Geach J. E., Smail I., Moran S. M., MacArthur L. A., Lagos C. d. P., Edge A. C., 2011, ApJ, 730, L19
Genzel R. et al., 2015, ApJ, 800, 20
Giovanelli R., Haynes M. P., 1985, AJ, 90, 2445
Giovanelli R. et al., 2005, AJ, 130, 2598
Gordon M. A., Baars J. W. M., Cocke W. J., 1992, A&A, 264, 337
Gutermuth R. A., Megeath S. T., Myers P. C., Allen L. E., Pipher J. L., Fazio G. G., 2009, ApJS, 184, 18
Haines C. P., Gargiulo A., La Barbera F., Mercurio A., Merluzzi P., Busarello G., 2007, MNRAS, 381, 7
Haynes M. P., Giovanelli R., Chincarini G. L., 1984, ARA&A, 22, 445
Hodge J. A., Carilli C. L., Walter F., Daddi E., Riechers D., 2013, ApJ, 776, 22
Hughes D. H. et al., 2010, in Stepp L. M., Gilmozzi R., Hall H. J., eds, Proc. SPIE Conf. Ser. Vol. 7733, Ground-based and Airborne Telescopes III. SPIE, Bellingham, p. 773312
Hwang H. S., Geller M. J., Diaferio A., Rines K. J., Zahid H. J., 2014, ApJ, 797, 106
Jablonka P., Combes F., Rines K., Finn R., Welch T., 2013, A&A, 557, A103
Jaffé Y. L. et al., 2011, MNRAS, 417, 1996
Jaffé Y. L., Poggianti B. M., Verheijen M. A. W., Deshev B. Z., van Gorkom J. H., 2012, ApJ, 756, L28

Jaffé Y. L., Poggianti B. M., Verheijen M. A. W., Deshev B. Z., van Gorkom J. H., 2013, MNRAS, 431, 2111

Jaffé Y. L., Smith R., Candlish G. N., Poggianti B. M., Sheen Y.-K., Verheijen M. A. W., 2015, MNRAS, 448, 1715

Jaffé A. et al., 2016, MNRAS, in press

Kenney J. D. P., Young J. S., 1989, ApJ, 344, 171

Kirkpatrick A. et al., 2014, ApJ, 796, 135

Krips M., Neri R., Cox P., 2012, ApJ, 753, 135

Kroupa P., 2001, MNRAS, 322, 231

Lagos C. D. P., Baugh C. M., Lacey C. G., Benson A. J., Kim H.-S., Power C., 2011, MNRAS, 418, 1649

Lagos C. d. P., Davis T. A., Lacey C. G., Zwaan M. A., Baugh C. M., Gonzalez-Perez V., Padilla N. D., 2014, MNRAS, 443, 1002

Lah P. et al., 2009, MNRAS, 399, 1447

Lee C., Chung A., Yun M. S., Cybulski R., Narayanan G., Erickson N., 2014, MNRAS, 441, 1363

Leroy A. K., Walter F., Brinks E., Bigiel F., de Blok W. J. G., Madore B., Thornley M. D., 2008, AJ, 136, 2782

Magdis G. E. et al., 2012, ApJ, 758, L9

Mahajan S., Haines C. P., Raychaudhury S., 2010, MNRAS, 404, 1745

Martin D. C. et al., 2005, ApJ, 619, L1

Mainzer A. et al., 2011, ApJ, 731, 53

Obreschkow D., Croton D., De Lucia G., Khochfar S., Rawlings S., 2009, ApJ, 698, 1467

Pappalardo C. et al., 2012, A&A, 545, A75

Poggianti B. M. et al., 2006, ApJ, 642, 188

Popping G., Somerville R. S., Trager S. C., 2014, MNRAS, 442, 2398

Popping G., Behroozi P. S., Peeples M. S., 2015, MNRAS, 449, 477

Rafieferantsoa M., Davé R., Anglés-Alcazar D., Katz N., Kollmeier J. A., Oppenheimer B. D., 2015, MNRAS, 453, 3980

Rasmussen J., Mulchaey J. S., Bai L., Ponman T. J., Raychaudhury S., Dariush A., 2012, ApJ, 757, 122

Rieke G. H. et al., 2004, ApJS, 154, 25

Rieke G. H., Alonso-Herrero A., Weiner B. J., Pérez-González P. G., Blaylock M., Donley J. L., Marcillac D., 2009, ApJ, 692, 556

Saintonge A. et al., 2011, MNRAS, 415, 32

Savitzky A., Golay M. J. E., 1964, Anal. Chem., 36, 1627

Schlegel D. J., Finkbeiner D. P., Davis M., 1998, ApJ, 500, 525

Scott T. C., Usero A., Brinks E., Boselli A., Cortese L., Bravo-Alfaro H., 2013, MNRAS, 429, 221

Scoville N. Z., Frayer D. T., Schinnerer E., Christopher M., 2003, ApJ, 585, L105

Scoville N. et al., 2007, ApJS, 172, 1

Scoville N. et al., 2013, ApJS, 206, 3

Snell R. L., Narayanan G., Yun M. S., Heyer M., Chung A., Irvine W. M., Erickson N. R., Liu G., 2011, AJ, 141, 38

Solomon P. M., Vanden Bout P. A., 2005, ARA&A, 43, 677

Stroe A., Oosterloo T., Röttgering H. J. A., Sobral D., van Weeren R., Dawson W., 2015, MNRAS, 452, 2731

Tacconi L. J. et al., 2010, Nature, 463, 781

Tran K.-V. H., Saintonge A., Moustakas J., Bai L., Gonzalez A. H., Holden B. P., Zaritsky D., Kautsch S. J., 2009, ApJ, 705, 809

Treu T., Ellis R. S., Kneib J.-P., Dressler A., Smail I., Czoske O., Oemler A., Natarajan P., 2003, ApJ, 591, 53

Verheijen M., van Gorkom J. H., Szomoru A., Dwarakanath K. S., Poggianti B. M., Schiminovich D., 2007, ApJ, 668, L9

Verheijen M. et al., 2010, preprint (arXiv:1009.0279)

Wang J. et al., 2015, MNRAS, 453, 2399

Wright E. L., 2006, PASP, 118, 1711

Wright E. L. et al., 2010, AJ, 140, 1868

York D. G. et al., 2000, AJ, 120, 1579

Young J. S., Scoville N. Z., 1991, ARA&A, 29, 581

Zavala J. A. et al., 2015, MNRAS, 452, 1140

Zibetti S., Charlot S., Rix H.-W., 2009, MNRAS, 400, 1181

APPENDIX A: SPECTRA

Here we present the spectra for all of our targets, sorted by decreasing signal-to-noise detections of the CO line by grouping them into reliable detections (Figs A1 and A2), marginal detections (Fig. A3), and non-detections (Figs A4 and A5). Alongside the CO spectra we show postage stamp images in the R band, with contours showing the MIPS [24] signal to noise, and the H I spectrum. Note that the CO spectra presented show the portion of the spectrum centred on ± 2 GHz around the expected frequency of the CO line, rather than the entire spectrum.

APPENDIX B: MCMC PARAMETER FITTING

In this section, we provide some example results of our MCMC fitting routine on the CO spectra for this study. In Figs B1 and B2, we plot the steps taken by the MCMC routine in exploring parameter space for the four parameters relevant to our Gaussian fitting to the CO spectra: (1) the amplitude, (2) central frequency, and (3) FWHM of the Gaussian, as well as (4) the D.C. offset. The plots show that after an initial period of exploring parameter space (the 'burn-in' depicted with black line segments) the code settles into the general areas best fitted by the Gaussian and samples the probabilities of those best-fitting parameters (in red). The final parameter fits, and their errors, come from the posterior distribution shown in red in these two figures.

APPENDIX C: COLD GASS GALAXY SIZES

In Fig. C1, we show a series of postage-stamp optical images of a selection of galaxies from the COLD GASS survey, along with the 22 arcsec beam FWHM used for their molecular gas determinations. These galaxies were selected randomly from the COLD GASS catalogue to sample the range of redshifts and physical sizes spanned by the sample. The COLD GASS survey has a mean redshift of $\bar{z} = 0.0365$ and a mean half-light radius (derived from the SDSS r' band) of $\bar{R}_{50} = 4.87$ arcsec. The 20 galaxies plotted in Fig. C1 consist of four sets of five random galaxies selected from each of the following quarters of the overall catalogue: (1) galaxies with $z < \bar{z}$ and $R_{50} < \bar{R}_{50}$, 2) galaxies with $z < \bar{z}$ & $R_{50} \geq \bar{R}_{50}$, 3) galaxies with $z \geq \bar{z}$ & $R_{50} < \bar{R}_{50}$, and 4) galaxies with $z \geq \bar{z}$ & $R_{50} \geq \bar{R}_{50}$.
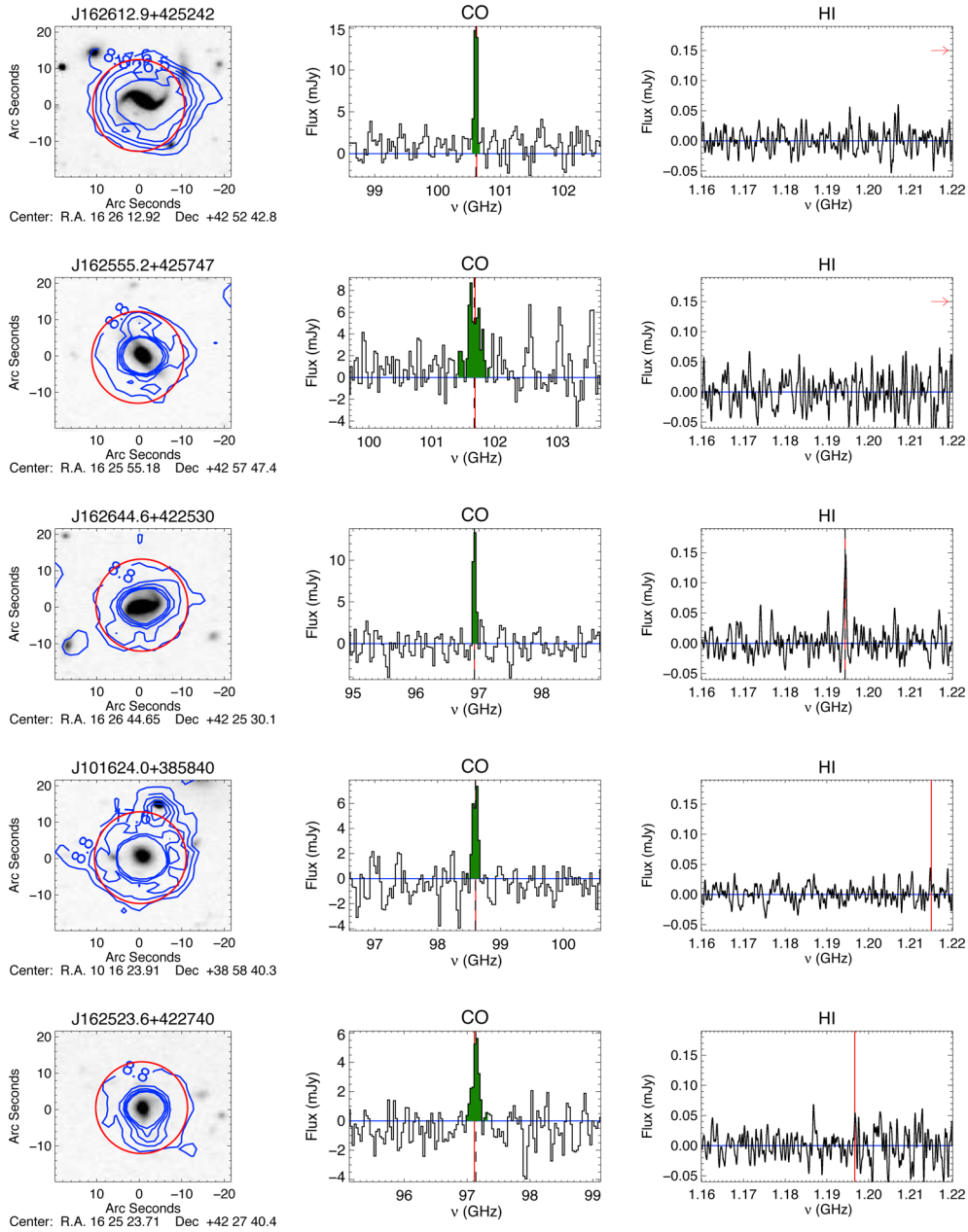
Figure A1. Each trio of panels corresponds to one of our target galaxies with a reliable detection of the CO line. The left-hand panels show the INT *R*-band maps centred on the galaxy. The red circle shows the RSR beam. In blue, we plot 5–25σ (in intervals of 5σ) contours from MIPS [24]. The middle panels give the CO spectrum showing the interval of ±2 GHz centred on the expected frequency of the CO line (shown in the vertical solid red line). The vertical dashed black line indicates the central frequency of the CO line from fitting a Gaussian (if detected). The right-hand panels show the H I spectrum, with the expected frequency indicated in red and the fitted H I frequency (if detected) with a dashed black line. A red arrow (left or right) indicates whether the expected H I line frequency is shorter, or longer, respectively, than the frequency range probed by the WSRT observations.
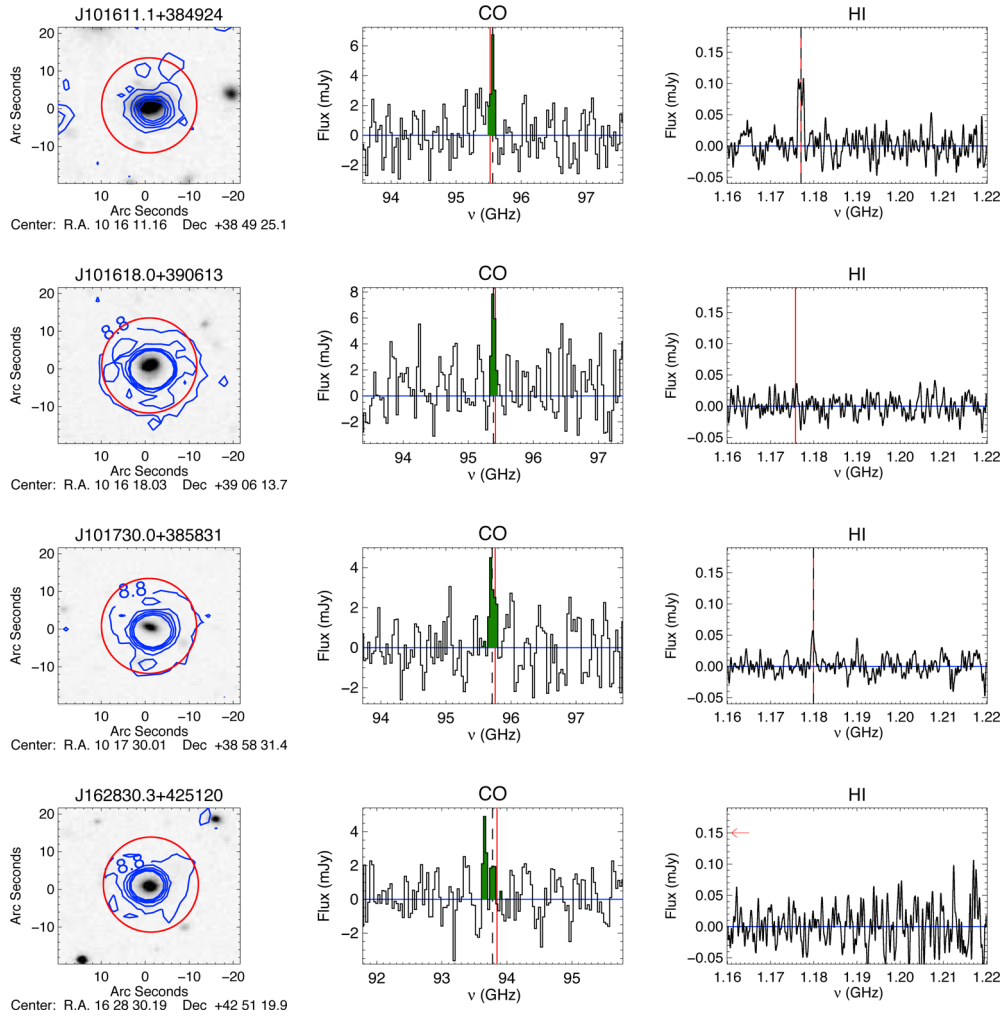
Figure A2. Each trio of panels corresponds to one of our target galaxies with a reliable detection of the CO line. The left-hand panels show the INT *R*-band maps centred on the galaxy. The red circle shows the RSR beam. In blue, we plot 5–25σ (in intervals of 5σ) contours from MIPS [24]. The middle panels give the CO spectrum showing the interval of ±2 GHz centred on the expected frequency of the CO line (shown in the vertical solid red line). The vertical dashed black line indicates the central frequency of the CO line from fitting a Gaussian (if detected). The right-hand panels show the H I spectrum, with the expected frequency indicated in red and the fitted H I frequency (if detected) with a dashed black line. A red arrow (left or right) indicates whether the expected H I line frequency is shorter, or longer, respectively, than the frequency range probed by the WSRT observations.
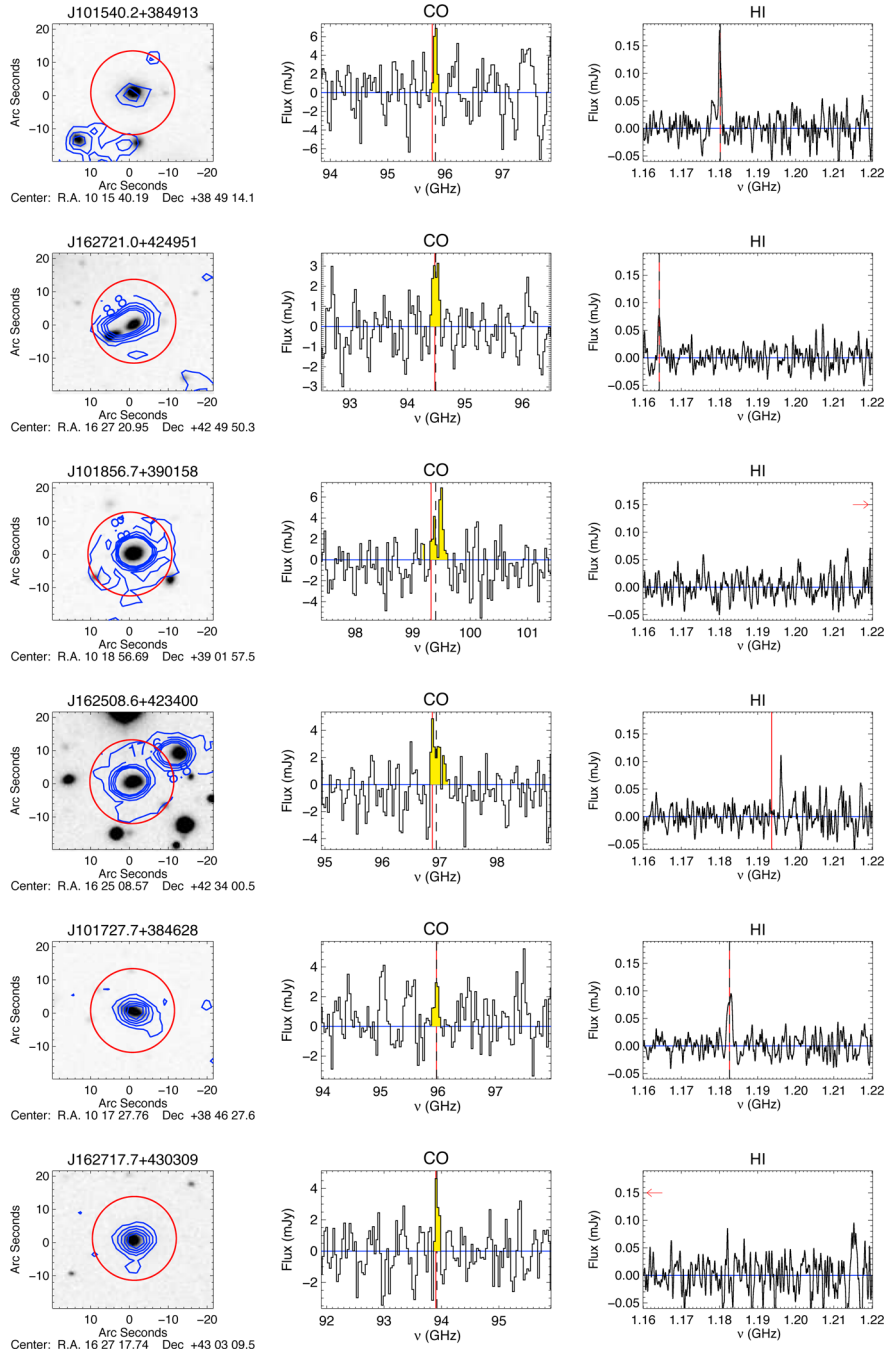
Figure A3. Each trio of panels corresponds to one of our target galaxies with a marginal detection of the CO line. The left-hand panels show the INT *R*-band maps centred on the galaxy. The red circle shows the RSR beam. In blue, we plot 5–25σ (in intervals of 5σ) contours from MIPS [24]. The middle panels give the CO spectrum showing the interval of ± 2 GHz centred on the expected frequency of the CO line (shown in the vertical solid red line). The vertical dashed black line indicates the central frequency of the CO line from fitting a Gaussian (if detected). The right-hand panels show the H I spectrum, with the expected frequency indicated in red and the fitted H I frequency (if detected) with a dashed black line. A red arrow (left or right) indicates whether the expected H I line frequency is shorter, or longer, respectively, than the frequency range probed by the WSRT observations.
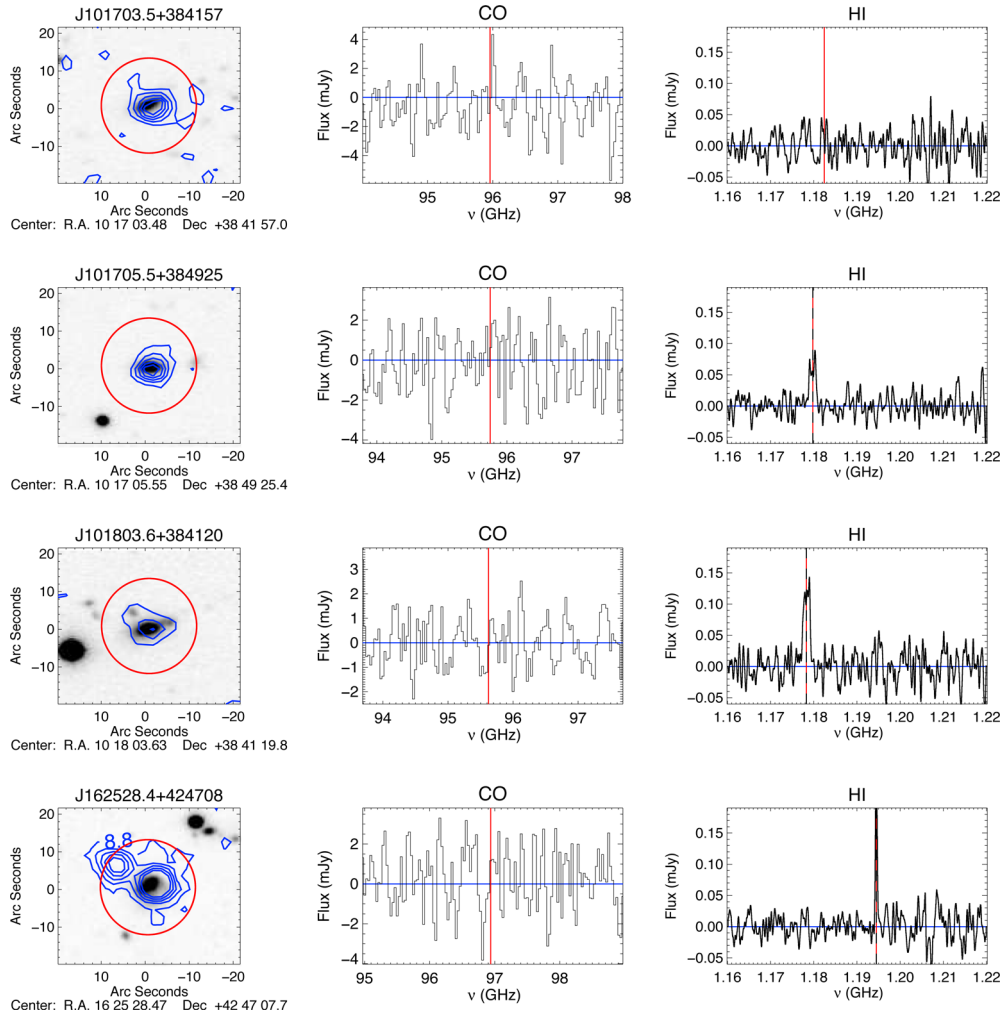
Figure A4. Each trio of panels corresponds to one of our target galaxies with a non-detection of the CO line. The left-hand panels show the INT *R*-band maps centred on the galaxy. The red circle shows the RSR beam. In blue, we plot 5–25σ (in intervals of 5σ) contours from MIPS [24]. The middle panels give the CO spectrum showing the interval of ±2 GHz centred on the expected frequency of the CO line (shown in the vertical solid red line). The vertical dashed black line indicates the central frequency of the CO line from fitting a Gaussian (if detected). The right-hand panels show the H I spectrum, with the expected frequency indicated in red and the fitted H I frequency (if detected) with a dashed black line. A red arrow (left or right) indicates whether the expected H I line frequency is shorter, or longer, respectively, than the frequency range probed by the WSRT observations.
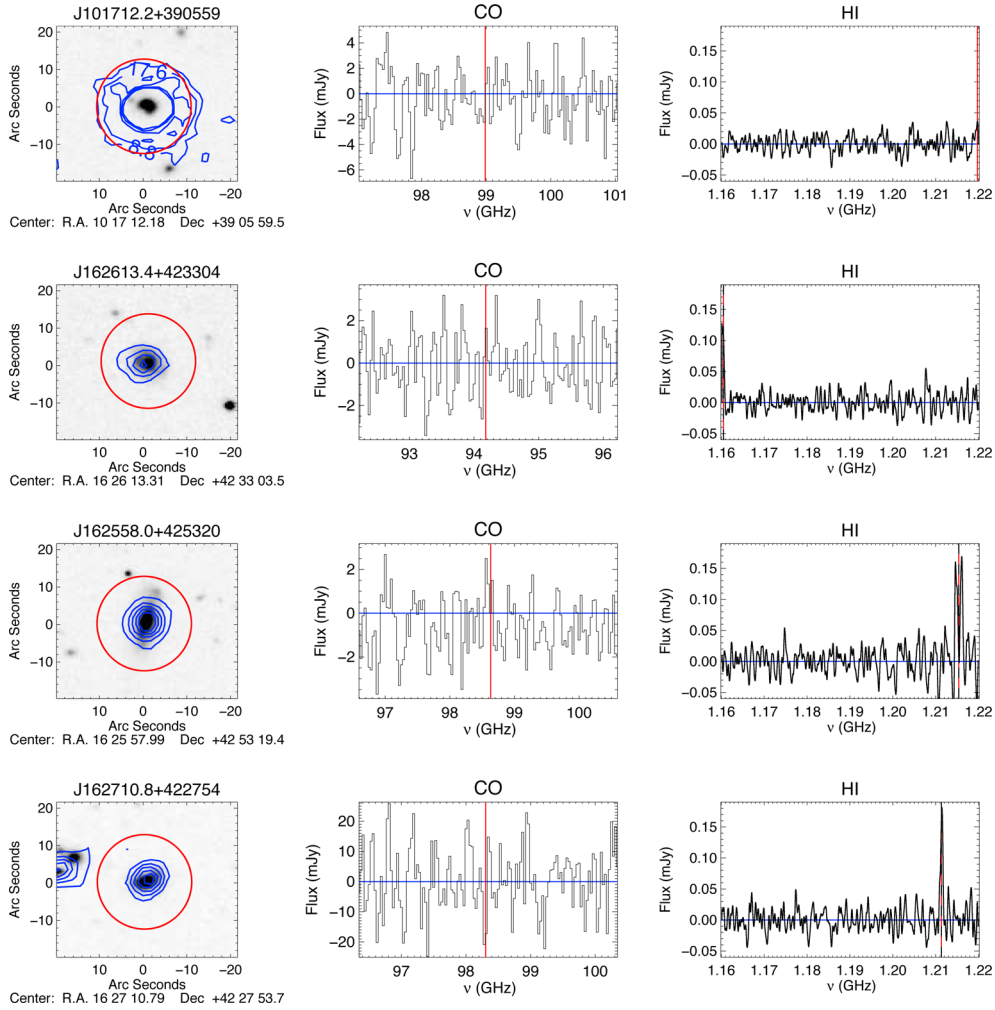
Figure A5. Each trio of panels corresponds to one of our target galaxies with a non-detection of the CO line. The left-hand panels show the INT *R*-band maps centred on the galaxy. The red circle shows the RSR beam. In blue, we plot 5–25σ (in intervals of 5σ) contours from MIPS [24]. The middle panels give the CO spectrum showing the interval of ± 2 GHz centred on the expected frequency of the CO line (shown in the vertical solid red line). The vertical dashed black line indicates the central frequency of the CO line from fitting a Gaussian (if detected). The right-hand panels show the H I spectrum, with the expected frequency indicated in red and the fitted H I frequency (if detected) with a dashed black line. A red arrow (left or right) indicates whether the expected H I line frequency is shorter, or longer, respectively, than the frequency range probed by the WSRT observations.
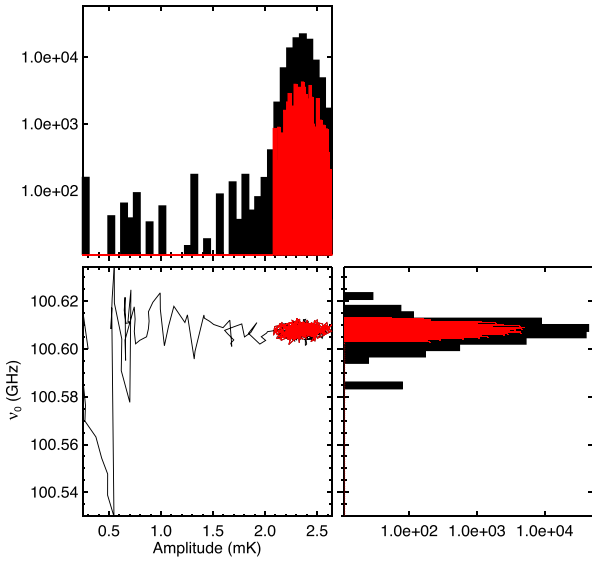
Figure B1. An example of exploring parameter space with the MCMC fitting code, for our target J162612.9+425242. The lower-left figure shows the values of amplitude and central frequency, initially for the 'burn-in' period in black but post burn-in is shown in red. Above is a histogram of the amplitude values overall (black) and post burn-in (red). The right rotated histogram shows a similar histogram for the central frequency.
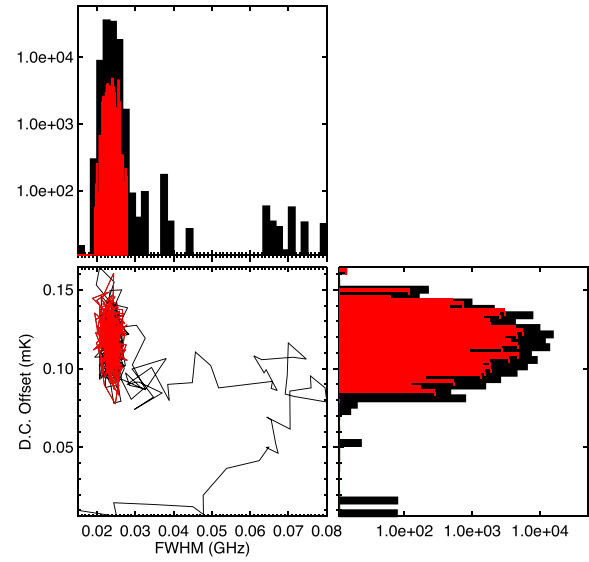
Figure B2. An example of exploring parameter space with the MCMC fitting code, for our target J162612.9+425242. The lower-left figure shows the values of the FWHM and D.C. offset, initially for the 'burn-in' period in black but post burn-in is shown in red. Above is a histogram of the FWHM values overall (black) and post burn-in (red). The right rotated histogram shows a similar histogram for the D.C. offset.
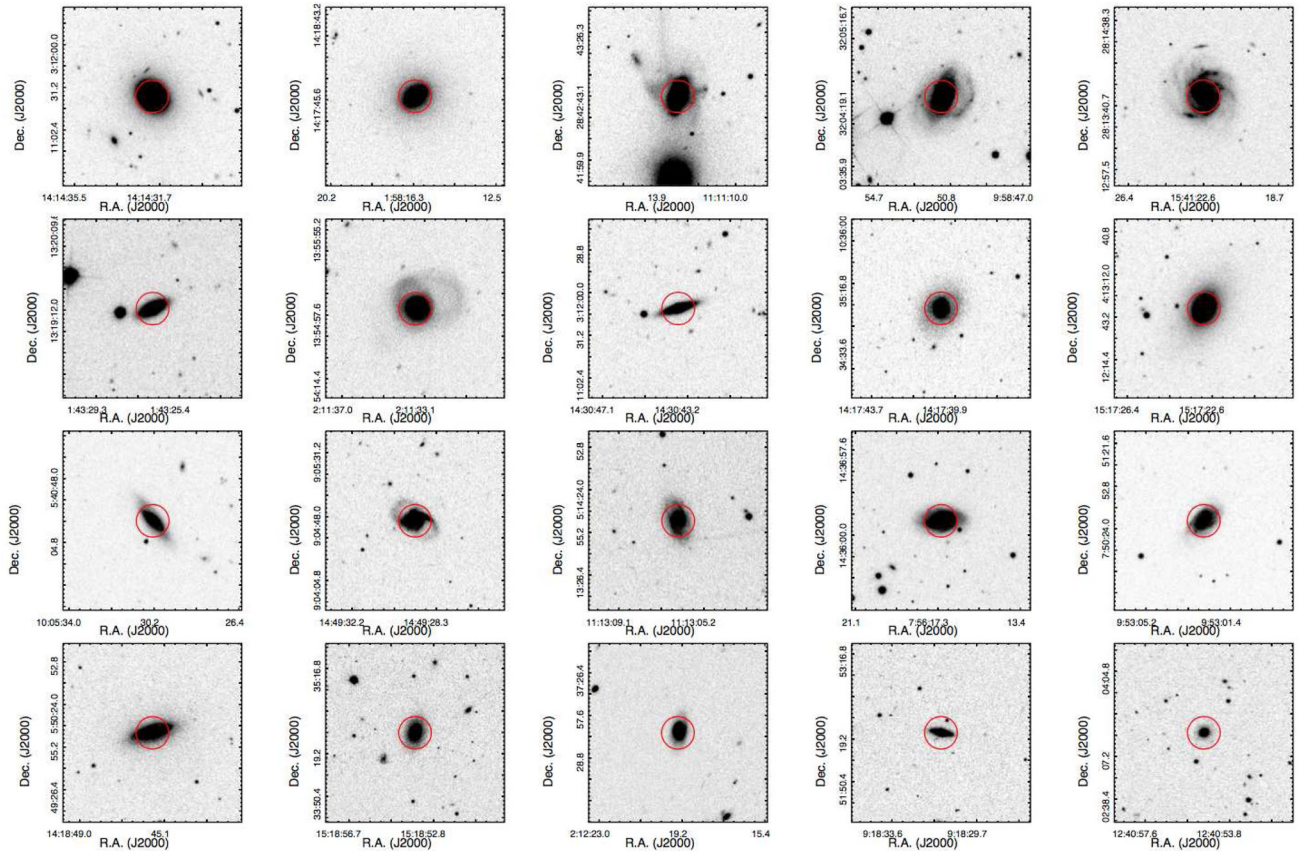

Figure C1. Random selection of galaxies from the COLD GASS survey. The images show the SDSS r' band, and the red circles are the 22 arcsec beam FWHM for CO observations in the COLD GASS study.

[1]*Department of Astronomy, University of Massachusetts, Amherst, MA 01003, USA*

[2]*SCiESMEX, Instituto de Geofísica, Unidad Michoacan, Universidad Nacional Autónoma de México, Morelia, Michoacan CP 58190, Mexico*

[3]*Instituto Nacional de Astrofísica, Óptica, y Electrónica (INAOE), Tonantzintla, Luis Enrique Erro 1, Sta. Ma. Tonantzintla, Puebla 72840, Mexico*

[4]*Consejo Nacional de Ciencia y Tecnología, Av. Insurgentes Sur 1582, Col. Credito Constructor, Del. Benito Juárez, CP 03940 Ciudad de México, D.F., Mexico*

[5]*Department of Astronomy, Yonsei University, 50 Yonsei-ro Seodaemun-gu, Seoul 120-749, Korea*

[6]*Department of Astronomy, Columbia University, Mail Code 5246, 550 W 120th St, NY 10027, USA*

[7]*Department of Physics and Astronomy, Rutgers University, 136 Frelinghuysen Road, Piscataway, NJ 08854, USA*

[8]*Departamento de Astronomía, Universidad de Chile, Casilla 36-D, Correo Central, Santiago 759124, Chile*

[9]*European Southern Observatory, Alonso de Cordova 3107, Vitacura, Casilla 19001, Santiago de Chile, Chile*

[10]*Department of Astronomy, Universidad de Concepción, Casilla 160-C, Concepción 3349001, Chile*

[11]*Dunlap Institute for Astronomy and Astrophysics, University of Toronto, 50 St George Street, Toronto, ON M5S 3H4, Canada*

[12]*INAF - Osservatorio Astronomico di Padova, vicolo dell Osservatorio 5, I-35122 Padova, Italy*

[13]*University of Groningen, Kapteyn Astronomical Institute, Landleven 12, NL-9747 AD Groningen, the Netherlands*

[14]*Tartu Observatory, Tõravere 61602, Estonia*

[15]*Institute of Physics, University of Tartu, Ravila 14c, Tartu 50411, Estonia*

[16]*Institute for Astronomy, University of Hawaii, Manoa, Hawaii 96822-1897, USA*

[17]*Canada-France-Hawaii Telescope Corp., Kamuela, Hawaii 96743-8432, USA*

This paper has been typeset from a TEX/LATEX file prepared by the author.